A consistent anisotropic damage model for laminated fiber-reinforced composites using the 3D-version of the Puck failure criterion

A consistent anisotropic damage model for laminated fiber-reinforced composites using the 3D-version of the Puck failure criterion

J. Reinoso[a,*], G. Catalanotti[b], A. Blázquez[a], P. Areias[c], P.P. Camanho[d], F. París[a]

[a] *Group of Elasticity and Strength of Materials, School of Engineering, University of Seville, Camino de los Descubrimientos s/n, 41092, Seville, Spain*

[b] *School of Mechanical and Aerospace Engineering, Queen's University Belfast, Ashby Building, Stranmillis Road, Belfast BT9 5AH, United Kingdom*

[c] *Department of Physics, University of Évora, Colégio Luís António Verney, Rua Romão Ramalho, 59, 7002-554 Évora, Portugal*

[d] *DEMec, Faculdade de Engenharia, Universidade do Porto, Rua Dr. Roberto Frias, 4200-465 Porto, Portugal*

Abstract

This paper presents a consistent anisotropic damage model for laminated fiber-reinforced composites relying on the 3D-version of the Puck failure criterion. The current model is based on ply failure mechanisms (fiber and inter-fiber failures) incorporating energetic considerations into the progressive damage evolution. The proposed formulation is implemented into the implicit FE commercial package ABAQUS using the user-defined capability `UMAT`. Additionally, the current damage model is combined with a locking-free solid shell formulation via the user-defined subroutine `UEL` in order to account for geometrical nonlinear effects in thin-walled applications. The reliability of the current formulation is first examined by means of several benchmark applications, and subsequently, the obtained numerical predictions are compared with experimental data corresponding to an open hole tension test. These applications show the practicability and accuracy of the proposed methodology for triggering damage in composite laminates, providing a robust modeling framework suitable for general specimens and loading conditions.

Keywords: A. Composite materials; B. FE-modeling; C. Damage modeling; D. Shells.

1. Introduction

The use of carbon and glass fiber-reinforced polymer (CFRP and GFRP, respectively) composites has gradually grown in several industrial sectors due to their superior mechanical performance over metals and metal-alloys. These materials have been incorporated for the production of aerospace and aeronautical components, rotor blades in wind-energy systems, automotive parts, among many other applications. The achievement of current demands of high-performance composite structures, especially with regard to their withstanding capabilities, requires the development of reliable modeling tools beyond initial localized failure, which can consider damage events stemming from different physical mechanisms.

Damage events in composite laminates can be categorized into two main groups: (i) interlaminar failure (delamination), and (ii) intralaminar failure (fiber and matrix breakage, fiber-matrix decohesion). Focusing on intralaminar failure, the initiation prediction is generally accomplished through strength-based failure criteria. In this setting, a large number of strain-based and stress-based damage criteria for laminated fiber-reinforced composites have been proposed in the last three-decades, see [14, 31, 39, 43, 52, 53, 55, 69, 71] and the references therein given. Initially, as a consequence of the geometric characteristics of laminates (thin and slender structures), the vast majority of the proposed failure criteria for composites were developed for

*Corresponding authors
Email address: `jreinoso@us.es` (J. Reinoso)

ply damage predictions under plane stress hypothesis. However, such an assumption can lead to inaccurate damage initiation prediction in complex stress states where the out-of-plane stress components (through the thickness) have a remarkable role. This is the case for instance of free-edges, open-holes, notched laminates, composite stiffened panels, among many other engineering applications [13, 30, 46, 58, 59, 64, 72]. With the aim of overcoming these limitations, more recently, a set of fully three-dimensional failure criteria for fiber-reinforced composites have been proposed, see the comprehensive revision carried out by Catalanotti and coauthors in [14]. In particular, several of these 3D failure criteria also incorporate geometric information with regard to failure by means of the so-called fracture plane concept.

Progressive damage modeling for composites has been a matter of intensive research in the last years, especially within the context of Finite Element Method (FEM). The numerical treatment of failure can be rooted on Continuum Damage Mechanics (CDM) [34] for irreversible processes, whereby the progressive loss of structural integrity can be triggered by means of a set of internal variables (usually known as damage variables) in a tractable manner [67]. The generalization of the basic concepts of CDM to composites usually accounts for tensorial-based representations of failure. Distinct damage formulations failing into this category (through second order or fourth order operators) have been adopted and applied to a wide range of engineering materials, see [2, 42, 47, 48, 75] to quote a few of them. One of the main difficulties associated with such tensorial descriptions regards the physical interpretation of the different damage variables therein employed. However, there exist a plausible alternative as is the development of phenomenological damage modeling for composites at lamina level. This latter approach is principally based on the description of the different damage mechanisms that characterize these materials. In this context, remarkable contributions are the landmark anisotropic damage model developed by Matzenmiller and coauthors [45] and the intensive research undertaken by Ladeveze and collaborators [37, 41]. These pioneering models exploited the definition of the complementary Gibbs free-energy function (thermodynamic potential) to set up the thermodynamic consistency and the corresponding finite element implementation. Alternative continuum damage models incorporating different ingredients into the phenomenological formulation have been proposed in the last years, see [23, 28, 30, 38, 43, 44, 65, 73], and more recently including nonlinear effects into the constitutive definition, see [25, 26, 27] and the references therein given.

From the numerical standpoint, modeling progressive failure provokes the well-known pathological mesh dependence due to strain localization events such as resulting from shear bands and damage accumulation, which has been generally remedied using the so-called crack-band approach [5]. This technique acts at the material (integration) point level by modifying the constitutive law through the introduction of a characteristic length parameter. Differing to the previous numerical strategy that is used at local level, a wide set of nonlocal computational techniques has been proposed in order to prevent this deficiency: (i) integral-based non-local formulations [36], (ii) gradient-enhanced strategies [51], among others. Some of these strategies have been subsequently adapted for composites models, see [29, 40].

In this investigation, a consistent anisotropic damage criterion for laminated fiber-reinforced composites using the 3D-version of the Puck failure criterion outlined in [55, 56] and subsequently implemented numerically in [23, 24] is developed. This failure theory was one of most accurate theories in the first and second world-wide failure exercises (WWFE-I and WWFE-II, respectively). The present formulation specifically addresses the thermodynamic consistency of the model by means of exploiting the additive decomposition of the Helmholtz free-energy function proposed in [76]. In addition, differing from previous Puck-based damage models, the formulation herein derived includes the following features: (i) the semi-empirical degradation rule originally proposed in [55, 56], which has been recently modified featuring a linear softening [25], is replaced by energetic considerations, (ii) instead of using the Mori–Tanaka Method (MTM) developed in Tandon and Weng [70] and applied to composites in [65], the consistent tangent operator is accordingly derived, and (iii) the proposed damage model is integrated into a solid shell element [10, 60], which allows a fully 3D constitutive definition at ply level to be performed. An essential characteristic of the proposed formulation is the remarkable simplicity with regard to its numerical implementation, leading to a consistent methodology especially suitable for large-scale computations involving thin-walled structures.

The manuscript is organized as follows. Section 2 outlines the theoretical formulation of the proposed constitutive model and revisits the 3D version of the Puck failure theory for fiber–reinforced composites. The fundamentals of the solid shell formulation, which makes use of the Enhanced Assumed Strain (EAS)

[68] and the Assumed Natural Strain (ANS) [5, 8] to alleviate locking pathologies, are addressed in Section 3. The principal details with regard to the FE implementation into the code ABAQUS [1] through the user-defined routines `UMAT` and `UEL` are described in Section 4. The predictive capabilities of the model are examined with respect to a set of benchmark and experimental applications in Section 5. Finally, the main conclusions of this investigation are given in Section 6.

2. Continuum damage model based on the Puck failure theory

2.1. Constitutive model

The vast majority of the existing damage models for laminated composites are founded on the fundamental basis of CDM [26, 28, 43, 45]. Through this modeling framework, the concept of effective stress, $\bar{\boldsymbol{\sigma}}$, is introduced. This effective stress state acts on the portion of resisting area A_{nd}, which is a portion of the original area, A, due to the initiation, growth and coalescence of micro-cracks. The basic expression that generally relates the effective and the actual Cauchy stress, $\boldsymbol{\sigma}$, reads:

$$\boldsymbol{\sigma} = (1-\mathfrak{d})\bar{\boldsymbol{\sigma}}; \qquad \boldsymbol{\sigma} = \mathbf{M}(\tilde{\mathfrak{d}}) : \bar{\boldsymbol{\sigma}}. \tag{1}$$

The expression given in Eq.$(1)_1$ defines an isotropic scalar-based damage model, $\mathfrak{d} \in [0,1)$, where $\mathfrak{d}=0$ represents the virgin material behavior, whereas $\mathfrak{d}=1$ identifies the fully deteriorated response. For an anisotropic tensorial-damage representation, Eq.$(1)_2$, the operator $\mathbf{M}(\tilde{\mathfrak{d}})$ denotes the so-called lamina damage tensor, where $\tilde{\mathfrak{d}}$ stands for a vector which collects the damage variables of the model.

To establish the thermodynamically consistent constitutive formulation that accounts for anisotropic damage, the decomposition of the Helmholtz free-energy function proposed by Wagner and Balzani [76] is here recalled. Complying with this strategy, the postulation of the Helmholtz free-energy function ($\Psi(\boldsymbol{\varepsilon}, \tilde{\mathfrak{d}})$) renders:

$$\Psi(\boldsymbol{\varepsilon}, \tilde{\mathfrak{d}}) = \sum_{i=f,m1,m2} (1-\mathfrak{d}_{it})(1-\mathfrak{d}_{ic})\Psi_i^e, \quad \text{with} \quad \Psi_i^e = \frac{1}{2}\boldsymbol{\varepsilon} : \mathbb{C}_i^e : \boldsymbol{\varepsilon}, \tag{2}$$

where Ψ_i^e stands for the elastic contributions; $\mathfrak{d}_{it}$ and $\mathfrak{d}_{ic}$ ($0 \leq \mathfrak{d}_{it}, \mathfrak{d}_{ic} \leq 1$) are scalar-valued damage variables in tension (subscript t) and in compression (subscript c), respectively; the subscripts f, $m1$ and $m2$ identify the damage variables associated with fiber failure (f) and matrix ($m1$ and $m2$) failures. These damage variables are collected in the damage vector $\tilde{\mathfrak{d}}$, which is defined as:

$$\tilde{\mathfrak{d}} = \sum_j \mathfrak{d}_j \;\; \text{with} \;\; j = \{ft, fc, m1t, m1c, m2t, m2c\}. \tag{3}$$

Through the assumption of a transversely isotropic response at the lamina level, the elastic constitutive operator $\mathbb{C}^e$ takes the form [20]:

$$\mathbb{C}^e = \partial_{\boldsymbol{\varepsilon}\boldsymbol{\varepsilon}}\Psi = \lambda \mathbf{1}\otimes\mathbf{1} + 2\mu_T\mathbb{I} + \alpha(\mathbf{1}\otimes\mathbf{A} + \mathbf{A}\otimes\mathbf{1}) + 2(\mu_L - \mu_T)\mathbb{I}_A + \beta\mathbf{A}\otimes\mathbf{A}, \tag{4}$$

where $\mathbf{1}$ and $\mathbb{I}$ are the second and the fourth order identity tensors, respectively; $\mathbf{A} := \mathbf{a}\otimes\mathbf{a}$ is the structural operator, where $\mathbf{a}$ coincides with the fiber direction; $\mathbb{I}_A = A_{im}\mathbb{I}_{jmkl} + A_{jm}\mathbb{I}_{mikl}$, and λ, α, β, μ_T and μ_L are the elastic constants, whose definitions are given in [74]. In the local material setting, the single elasticity matrices in Voigt notation $\mathbb{C}_i^e$ are defined by:

$$\mathbb{C}_f^e = \begin{bmatrix} \mathbb{C}_{11}^e & 0 & 0 & 0 & 0 & 0 \\ 0 & 0 & 0 & 0 & 0 & 0 \\ 0 & 0 & 0 & 0 & 0 & 0 \\ 0 & 0 & 0 & 0 & 0 & 0 \\ 0 & 0 & 0 & 0 & 0 & 0 \\ 0 & 0 & 0 & 0 & 0 & 0 \end{bmatrix}; \; \mathbb{C}_{m1}^e = \begin{bmatrix} 0 & \mathbb{C}_{12}^e & \mathbb{C}_{13}^e & 0 & 0 & 0 \\ \mathbb{C}_{21}^e & \mathbb{C}_{22}^e & \mathbb{C}_{23}^e & 0 & 0 & 0 \\ \mathbb{C}_{31}^e & \mathbb{C}_{32}^e & \mathbb{C}_{33}^e & 0 & 0 & 0 \\ 0 & 0 & 0 & 0 & 0 & 0 \\ 0 & 0 & 0 & 0 & 0 & 0 \\ 0 & 0 & 0 & 0 & 0 & \mathbb{C}_{66}^e \end{bmatrix}; \; \mathbb{C}_{m2}^e = \begin{bmatrix} 0 & 0 & 0 & 0 & 0 & 0 \\ 0 & 0 & 0 & 0 & 0 & 0 \\ 0 & 0 & 0 & 0 & 0 & 0 \\ 0 & 0 & 0 & \mathbb{C}_{44}^e & 0 & 0 \\ 0 & 0 & 0 & 0 & \mathbb{C}_{55}^e & 0 \\ 0 & 0 & 0 & 0 & 0 & 0 \end{bmatrix} \tag{5}$$

Analyzing the sub-matrices introduced in Eq.(5), it can be observed that:

- The sub-matrix $\mathbb{C}_f^e$ decouples normal contribution associated with the fiber direction.
- The term associated with $\mathbb{C}_{m1}^e$ incorporates: (i) the part of the elastic constitutive tensor transverse to the fiber direction, (ii) the coupling between the normal and transverse actions to the fiber direction, and (ii) the transverse/transverse tangential effects to the fiber.
- The sub-matrix $\mathbb{C}_{m2}^e$ accounts for the parallel/transverse shear contributions to the fiber.

The local dissipation Clausius-Plank inequality under isothermal conditions can be expressed as [33]:

$$\mathcal{D}_{int} = \boldsymbol{\sigma} : \dot{\boldsymbol{\varepsilon}} - \dot{\Psi} \geq 0 \tag{6}$$

The time derivative of the free-energy function defined in Eq.(2) yields:

$$\dot{\Psi} = \sum_{i=f,m1,m2} (1-\mathfrak{d}_{it})(1-\mathfrak{d}_{ic}) \frac{\partial \Psi_i^e}{\partial \boldsymbol{\varepsilon}} : \dot{\boldsymbol{\varepsilon}} - \sum_{i=f,m1,m2} (1-\mathfrak{d}_{ic}) \Psi_i^e \dot{\mathfrak{d}}_{it} - \sum_{i=f,m1,m2} (1-\mathfrak{d}_{it}) \Psi_i^e \dot{\mathfrak{d}}_{ic}. \tag{7}$$

Substituting Eq.(7) into Eq.(6) leads to:

$$\mathcal{D}_{int} = \left[\boldsymbol{\sigma} - \sum_{i=f,m1,m2} (1-\mathfrak{d}_{it})(1-\mathfrak{d}_{ic}) \partial_{\boldsymbol{\varepsilon}} \Psi_i^e \right] : \dot{\boldsymbol{\varepsilon}} + \sum_{i=f,m1,m2} (1-\mathfrak{d}_{ic}) \Psi_i^e \dot{\mathfrak{d}}_{it} + \sum_{i=f,m1,m2} (1-\mathfrak{d}_{it}) \Psi_i^e \dot{\mathfrak{d}}_{ic} \geq 0. \tag{8}$$

Note that this condition must hold for every admissible process. The Cauchy stress tensor is defined as [20]:

$$\boldsymbol{\sigma} := \sum_{i=f,m1,m2} (1-\mathfrak{d}_{it})(1-\mathfrak{d}_{ic}) \partial_{\boldsymbol{\varepsilon}} \Psi_i^e = \sum_{i=f,m1,m2} (1-\mathfrak{d}_{it})(1-\mathfrak{d}_{ic}) \bar{\boldsymbol{\sigma}}_i, \tag{9}$$

where $\bar{\boldsymbol{\sigma}}_i$ is the effective stress tensor associated with the decomposed scheme defined in Eq.(5). Using the considerations outlined in Eq.(9), the dissipation inequality renders:

$$\mathcal{D}_{int} = \sum_{i=f,m1,m2} (1-\mathfrak{d}_{ic}) \Psi_i^e \dot{\mathfrak{d}}_{it} + \sum_{i=f,m1,m2} (1-\mathfrak{d}_{it}) \Psi_i^e \dot{\mathfrak{d}}_{ic} \geq 0. \tag{10}$$

The consistency of the proposed model is ensured as long as the evolution of the damage state variables in non-negative, i.e. $\dot{\mathfrak{d}}_{it} \geq 0$ and $\dot{\mathfrak{d}}_{ic} \geq 0$. Therefore, the self-healing of the material along the loading history is avoided. This condition is fulfilled by means of the definition of the evolution equations for each of the damage variables herewith considered.

The thermodynamic driving damage forces under tensile, $\mathcal{Y}_{it}$, and compressive, $\mathcal{Y}_{ic}$, conditions, which are conjugate to the pairs $\mathfrak{d}_{it}$ and $\mathfrak{d}_{ic}$, respectively, are defined as:

$$\mathcal{Y}_{it} = \frac{\partial \Psi}{\partial \mathfrak{d}_{it}}; \quad \mathcal{Y}_{ic} = \frac{\partial \Psi}{\partial \mathfrak{d}_{ic}}; \tag{11}$$

To provide a physical interpretation, we postulate the damage energy dissipated as:

$$\frac{\mathcal{G}_j}{L_c} = \int_0^\infty \mathcal{Y}_j \dot{\mathfrak{d}}_j \, \mathrm{d}t. \quad j = ft, fc, m1t, m1c, m2t, m2c; \tag{12}$$

where L_c is the characteristic element size of the corresponding spatial discretization (FE mesh). This parameter is introduced in order to minimize the dependency of the computational results with respect to the underlying FE discretization according to the crack band approach [5].

The current damage model requires several intralaminar fracture parameters as input data: (i) $\mathcal{G}_{ft}$ and $\mathcal{G}_{fc}$ which are the fiber fracture energies in tension and in compression, respectively, (ii) $\mathcal{G}_{m1t}$ and $\mathcal{G}_{m1c}$ which correspond to the fracture energies transverse to the fiber direction in tension and in compression, respectively, and (iii) the shear fracture energy $\mathcal{G}_{m2}$. The determination of such fracture energies can

be accomplished by means of Fracture Mechanics-based tests [15, 16, 17, 54]. Tensile failure along the transverse direction, $\mathcal{G}_{m1t}$ can be estimated using a double cantilever beam (DCB) test [50]. The fracture energy corresponding to shear failure $\mathcal{G}_{m2}$ is generally determined by using the four–point end notched flexure test (4-ENF) [43]. As was thoroughly discussed in [26, 43], the determination of the fracture energies associated with compressive loading states is notable more complicated.

Through the previous definitions, the damaged constitutive relation takes the form:

$$\mathbb{C}(\tilde{\mathfrak{d}}) = \begin{bmatrix} (1-\mathfrak{d}_f)\mathbb{C}^e_{11} & (1-\mathfrak{d}_{m1})\mathbb{C}^e_{12} & (1-\mathfrak{d}_{m1})\mathbb{C}^e_{13} & 0 & 0 & 0 \\ (1-\mathfrak{d}_{m1})\mathbb{C}^e_{21} & (1-\mathfrak{d}_{m1})\mathbb{C}^e_{22} & (1-\mathfrak{d}_{m1})\mathbb{C}^e_{23} & 0 & 0 & 0 \\ (1-\mathfrak{d}_{m1})\mathbb{C}^e_{31} & (1-\mathfrak{d}_{m1})\mathbb{C}^e_{32} & (1-\mathfrak{d}_{m1})\mathbb{C}^e_{33} & 0 & 0 & 0 \\ 0 & 0 & 0 & (1-\mathfrak{d}_{m2})\mathbb{C}^e_{44} & 0 & 0 \\ 0 & 0 & 0 & 0 & (1-\mathfrak{d}_{m2})\mathbb{C}^e_{55} & 0 \\ 0 & 0 & 0 & 0 & 0 & (1-\mathfrak{d}_{m1})\mathbb{C}^e_{66} \end{bmatrix} \tag{13}$$

with

$$(1-\mathfrak{d}_f) = (1-\mathfrak{d}_{ft})(1-\mathfrak{d}_{fc}); \;\; (1-\mathfrak{d}_{m1}) = (1-\mathfrak{d}_{m1t})(1-\mathfrak{d}_{m1c}); \;\; (1-\mathfrak{d}_{m2}) = (1-\mathfrak{d}_{m2t})(1-\mathfrak{d}_{m2c}) \tag{14}$$

2.2. Failure criterion: fundamentals of the Puck failure theory

The current damage model is formulated at the ply level, where the ply coordinates are denoted by the local setting $0-\mathbf{e}_1-\mathbf{e}_2-\mathbf{e}_3$, see Figure 1.a. In what follows, fiber-direction is identified by the symbol $\parallel$ (subscript 1), whilst transverse to the fiber direction in-plane (subscript 2) and out-of-plane (subscript 3) are denoted by the symbol $\perp$. Material nonlinearity is attained through the development of brittle cracks at the lamina level [23, 24, 56], and damage growth is formulated based on the thermodynamic considerations given in Section 2.1.

2.2.1. Damage activation functions

Puck's failure theory for fiber-reinforced composites distinguishes two failure mechanisms: (i) inter-fibre fracture (IFF) and (ii) fibre fracture (FF). In particular, the current formulation is also equipped with the distinction between damage development under tensile and compressive conditions [25]. The elastic domain is accordingly characterized by the definition of four damage surfaces: (i) tensile/compressive fiber (longitudinal) failure, and (ii) tensile/compressive inter-fiber (transverse) failure. The damage activation functions (F_N) associated with fiber failure in tension and in compression ($N = FF+, FF-$) and inter-fiber failure in tension and in compression ($N = IFF+, IFF-$) adopt the forms:

$$F_{FF+} = f_{E,FF+} - r_{E,FF+} \leq 0; \quad F_{FF-} = f_{E,FF-} - r_{E,FF-} \leq 0 \tag{15}$$

$$F_{IFF+} = f_{E,IFF+} - r_{E,IFF+} \leq 0; \quad F_{IFF-} = f_{E,IFF-} - r_{E,IFF-} \leq 0, \tag{16}$$

where $f_{E,FF+}$ and $f_{E,FF-}$ are the fiber failure exposure factors (also denominated as factors of efforts [65]) in tension and in compression, respectively, whereas $r_{E,FF+}$ and $r_{E,FF-}$ are the fiber damage thresholds in tension and in compression, respectively; $f_{E,IFF+}$ and $f_{E,IFF-}$ are the inter-fiber failure the exposure factors in tension and in compression, respectively, whereas $r_{E,IFF+}$ and $r_{E,IFF-}$ identify the inter-fiber damage thresholds in tension and in compression, respectively. Note that each of the previous damage thresholds is initially set to 1, that corresponds to the value of failure exposure factors that indicate damage onset.

Failure exposure factors relate the length of a pseudo vector $\{\bar{\boldsymbol{\sigma}}\}$ and that corresponding to the fracture vector $\{\bar{\boldsymbol{\sigma}}_{(fr)}\}$, i.e. $f_E = \{\bar{\boldsymbol{\sigma}}\}/\{\bar{\boldsymbol{\sigma}}_{(fr)}\}$, see Figure 1.b [23]. Upon damage is initiated, the corresponding exposure factor increases with damage progression, which is accounted for via the associated damage variable. Throughout the loading history, damage thresholds are treated as internal model variables in the computational model, since they delimit the elastic domain at each time step, see Section 2. It is also noteworthy that, in contrast to precedent models where a empirical stiffness degradation rule is assumed [23, 65], the present formulation incorporates energetic considerations to determine the released energy along the damage process [43, 44], see Section 2.2.2.

The exposure factors corresponding to fiber failure previously introduced in Eq.(15) render:

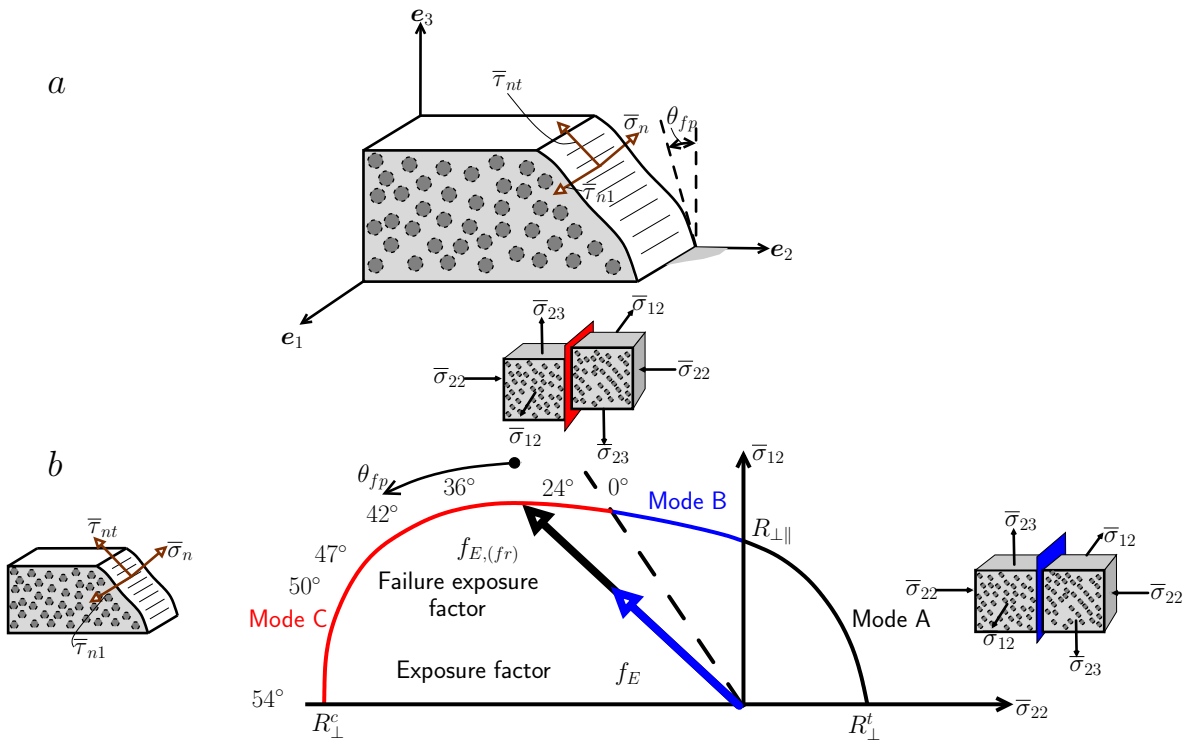

Figure 1: (a) Action plane concept: definition of acting stresses (stressing) on the fracture plane whose angle is denoted by θ_{fp}. (b) Visualization of the exposure factor f_E, where $f_{E,(fr)}$ is the exposure factor at the failure point. Adaptation from [23].

- Fiber failure (FF) in tension:

$$f_{E,FF+} = \frac{1}{R^t_{\parallel}} \left[\bar{\sigma}_{11} - \left(\nu_{\perp\parallel} - \frac{E_{\parallel}}{E_{\parallel f}} \nu_{\perp\parallel f} \right) (\bar{\sigma}_{22} + \bar{\sigma}_{33}) \right] \tag{17}$$

- Fiber failure (FF) in compression:

$$f_{E,FF-} = \frac{1}{R^c_{\parallel}} \left[\bar{\sigma}_{11} - \left(\nu_{\perp\parallel} - \frac{E_{\parallel}}{E_{\parallel f}} \nu_{\perp\parallel f} m_{\sigma f} \right) (\bar{\sigma}_{22} + \bar{\sigma}_{33}) \right] \tag{18}$$

where $R^t_{\parallel}$, $R^c_{\parallel}$ are the tensile and compressive longitudinal strengths, respectively; $E_{\parallel}$ and $E_{\parallel f}$ are the elastic properties of the lamina in fiber direction and the fibres, respectively; $\nu_{\perp\parallel}$ and $\nu_{\perp\parallel f}$ identify the Poisson's ratios of the lamina and the fibres, respectively; $m_{\sigma f}$ stands for the so-called magnification factor (which is assumed to take the values to 1.3 for GFRC and 1.1 for CFRC [23]).

According to the experimental evidences, Puck and coworkers formulated a failure criterion for inter-fiber failure assuming that the fracture is mainly provoked by the stress components acting on the so-called fracture plane [23, 24, 56], see Figure 1.a. These authors specifically differentiates between the fracture and action planes concepts, whose local orientation are not necessarily coincident. The respective orientations of the action and fracture planes are denoted by θ and θ_{fp} in the sequel.

On the action plane, a set of local stresses associated with this plane are given by: $\{\bar{\sigma}_n(\theta), \bar{\tau}_{nt}(\theta), \bar{\tau}_{n1}(\theta)\}$, where $\bar{\sigma}_n(\theta)$ is the stress component normal to the action plane, $\bar{\tau}_{nt}(\theta)$ denotes the shear stress component on the action plane transverse to the fiber, and $\bar{\tau}_{n1}(\theta)$ identifies the shear stress component on the action plane parallel to the fiber, with $\tau_{n\psi} = \sqrt{\bar{\tau}^2_{nt} + \bar{\tau}^2_{n1}}$.

For arbitrary loading conditions, the orientation of the fracture plane should be determined by evaluating the inter-fiber failure criterion based on the local setting associated with each of the potential fracture planes. Note that, although for the case of pure uniaxial compression loading the fracture through the thickness might be expected with an orientation of 45° (where the maximum shear stress should occur), experimental evidences show that this angle is about $\theta_{fp} = 53° \pm 2°$. In spite of an explanation of this fact based on internal friction [23, 56], Correa and coauthors [21, 22] presented an alternative elucidation of this phenomenon relying on micromechanical considerations.

The effective local stress components on the fracture plane can be expressed in terms of the lamina effective stress components $\bar{\boldsymbol{\sigma}}$ as follows:

$$\begin{bmatrix} \bar{\sigma}_n(\theta) \\ \bar{\tau}_{nt}(\theta) \\ \bar{\tau}_{n1}(\theta) \end{bmatrix} = \begin{bmatrix} \cos^2\theta & \sin^2\theta & 2\cos\theta\sin\theta & 0 & 0 \\ -\cos\theta\sin\theta & \cos\theta\sin\theta & \cos^2\theta - \sin^2\theta & 0 & 0 \\ 0 & 0 & 0 & \sin\theta & \cos\theta \end{bmatrix} \begin{bmatrix} \bar{\sigma}_{22} \\ \bar{\sigma}_{33} \\ \bar{\sigma}_{23} \\ \bar{\sigma}_{13} \\ \bar{\sigma}_{12} \end{bmatrix}. \tag{19}$$

The central idea developed by Puck states that only the three stress (stressing) components on the so-called acting plane $\{\bar{\sigma}_\perp, \bar{\tau}_{\perp\parallel}, \bar{\tau}_{\perp\perp}\}$, which respectively identify the stress components normal to that plane, the in-plane shear and the out-of-plane shear components, provoke the failure. Then, three fracture strengths on the fracture plane (identified by the superscript A) should be determined: $R^{At}_\perp$, $R^A_{\perp\perp}$ and $R^A_{\perp\parallel}$, whereby one can identify $R^{At}_\perp = R^t_\perp$ and $R^A_{\perp\parallel} = R_{\perp\parallel}$, where $R^t_\perp$ and $R_{\perp\parallel}$ denote the tensile strength transverse to the fiber and the in-plane shear strength, respectively [23]. The fracture strength $R^A_{\perp\perp}$ is defined as follows:

$$R^A_{\perp\perp} = \frac{R^c_\perp}{2(1 + p^c_{\perp\perp})}, \tag{20}$$

where $R^c_\perp$ is the compressive strength transverse to the fiber and $p^c_{\perp\perp}$ is an inclination parameter whose meaning is comprehensively discussed in [55, 56].

With the previous definitions at hand, the exposure factors corresponding to inter-fiber failure (IFF) introduced in Eq.(16) take the form [23, 24]:

- Inter-fiber failure (IFF) in tension:

$$f_{E,IFF+}(\theta) = \sqrt{\left[\left(\frac{1}{R^{At}_\perp} - \frac{p^t_{\perp\psi}}{R^A_{\perp\psi}}\right)\bar{\sigma}_n(\theta)\right]^2 + \left(\frac{\bar{\tau}_{nt}(\theta)}{R^A_{\perp\perp}}\right)^2 + \left(\frac{\bar{\tau}_{n1}(\theta)}{R^A_{\parallel\perp}}\right)^2} + \frac{p^t_{\perp\psi}}{R^A_{\perp\psi}}\bar{\sigma}_n(\theta) \quad \text{for} \quad \bar{\sigma}_n \geq 0 \tag{21}$$

- Inter-fiber failure (IFF) in compression:

$$f_{E,IFF-}(\theta) = \sqrt{\left(\frac{p^c_{\perp\psi}}{R^A_{\perp\psi}}\bar{\sigma}_n(\theta)\right)^2 + \left(\frac{\bar{\tau}_{nt}(\theta)}{R^A_{\perp\perp}}\right)^2 + \left(\frac{\bar{\tau}_{n1}(\theta)}{R^A_{\parallel\perp}}\right)^2} + \frac{p^c_{\perp\psi}}{R^A_{\perp\psi}}\bar{\sigma}_n(\theta) \quad \text{for} \quad \bar{\sigma}_n < 0 \tag{22}$$

with

$$\cos^2\psi = \frac{\bar{\tau}^2_{nt}}{\bar{\tau}^2_{nt} + \bar{\tau}^2_{n1}}; \quad \sin^2\psi = \frac{\bar{\tau}^2_{n1}}{\bar{\tau}^2_{nt} + \bar{\tau}^2_{n1}}. \tag{23}$$

The orientation of the fracture plane is identified with the plane with the highest exposure fracture, whilst the recommended material-dependent inclination parameters $p^t_{\perp\perp}$ $p^c_{\perp\perp}$, $p^t_{\perp\parallel}$ $p^c_{\perp\parallel}$ that characterize the master fracture body (MFB) of the Puck criterion are listed in Table 1 for glass fiber-reinforced (GFRP) and carbon fiber-reinforced (CFRP) composites.

The definition of the inclination parameters $p^t_{\perp\psi}$ and $p^c_{\perp\psi}$ at any angle ψ are given by the following relations:

$$\frac{p^i_{\perp\psi}}{R^A_{\perp\psi}} = \frac{p^i_{\perp\perp}}{R^A_{\perp\perp}}\cos^2\psi + \frac{p^i_{\perp\parallel}}{R^A_{\perp\parallel}}\sin^2\psi, \;\; i = t, c; \tag{24}$$

Material	$p^t_{\perp\perp}$	$p^c_{\perp\perp}$	$p^t_{\perp\parallel}$	$p^c_{\perp\parallel}$
GFRP	0.30	0.25	0.20	0.25
CFRP	0.35	0.30	0.25	0.30

Table 1: Recommended inclination factors for glass fiber-reinforced (GFRP) and carbon fiber-reinforced (CFRP) composites.

with

$$R^A_{\perp\psi} = \left[\left(\frac{\cos\psi}{R^A_{\perp\perp}} \right)^2 + \left(\frac{\sin\psi}{R^A_{\perp\parallel}} \right)^2 , \right] \tag{25}$$

Relying on the numerical and experimental investigations conducted by Correa et al. [21, 22], in order to have a more representative failure criterion with respect to the experimental evidences, the influence of the stress component parallel to the fiber $\bar{\sigma}_{11}$ is considered through introducing a weakening factor η_w into the definition of the IFF exposure factor. The new definition of $f_{E,IFF\pm}$ reads:

$$f_{E,IFF\pm} = \frac{f_{E,IFF\pm}}{\eta_w} \quad \text{with} \quad \eta_w = \sqrt{1 - \frac{(1 - f_{E,FF})^2}{a^2}} \tag{26}$$

where

$$a = \frac{1 - s}{\sqrt{1 - m^2}} \tag{27}$$

An elliptic form of the so-called Puck's fracture cigar through the plane $(\bar{\sigma}_{11} - \bar{\sigma}_{22})$ for $m = 0.5$ accounts for the interaction between FF and IFF modes depending on the values of m and s [55, 56]. Due to the lack of experimental data, it is recommended to take $m = s = 0.5$. With these values, the factor a in Eq.(27) can be computed and correspondingly $f_{E,IFF\pm}$ through Eq.(26).

2.2.2. Damage evolution

The evolution of the previously introduced damage variables can be defined by the rate equations:

$$\dot{\mathfrak{d}}_N = \dot{\varsigma}_N \phi(f_{E,N}, \mathfrak{d}_N) \quad \dot{r}_N = \dot{\varsigma}_N \qquad N = \{FF+, FF-, IFF+, IFF-\}. \tag{28}$$

In the previous expression, $\dot{\varsigma}_N$ is a damage consistency parameter associated with the damage mechanism identified by the subscript N, and $\phi(f_{E,N}, \mathfrak{d}_N)$ is a dissipation function. The damage consistency parameter allows the definition of the loading/unloading conditions by means of the Kuhn-Tucker conditions to be performed:

$$\dot{r}_N \geq 0; \quad F_N \leq 0; \quad \dot{r}_N F_N = 0. \tag{29}$$

The conditions outlined in Eq.(29) state that while $F_N \leq 0$, the damaged criterion is not fulfilled, and according to Eq.$(29)_3$ no damage evolution takes place ($\dot{r}_N = 0$). Conversely, $\dot{r}_N > 0$ implies damage progression, and the following consistency condition should be satisfied:

$$\dot{F}_N = \dot{f}_{E,N} - \dot{r}_N = 0. \tag{30}$$

The evolution of the elastic space for each of the failure mechanisms considered in the present model is given by the expression [67, 43]:

$$r_N = \max\{1, \max_{s=0,t} f_{E,N}\}. \tag{31}$$

The evolution of the damage state variables can obey distinct softening profiles such linear and exponential laws, among many others, see [26, 27, 38] and the references therein given. In this investigation, the exponential degradation laws proposed in Maimí et al. [43, 44] are considered to account for progressive stiffness degradation (Figure 2). These degradation laws are generally expressed as:

$$\mathfrak{d}_{fj} = 1 - \frac{1}{f_{E,FF}} \exp\left[A^j_f (1 - f_{E,FF}) \right] \quad j = t, c; \tag{32}$$

$$\mathfrak{d}_{mij} = 1 - \frac{1}{f_{E,FF}} \exp\left[A^j_{mi}(1 - f_{E,IFF})\right] \quad i = 1,2; \;\; j = t,c. \tag{33}$$

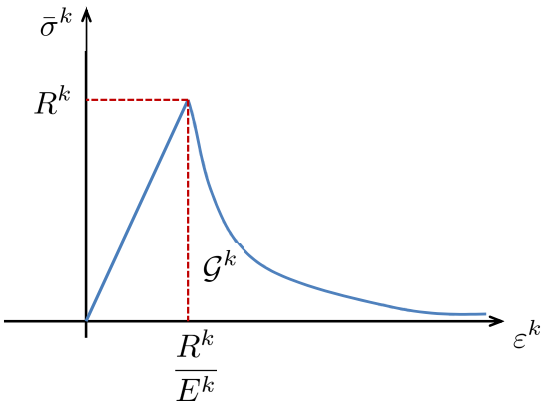

Figure 2: Damage evolution law according to exponential softening. E^k is an undamage elastic property associated with the stress and the strain component $\bar{\sigma}^k$ and ε^k; R^k is the associated strength, whilst $\mathcal{G}^k$ denotes the corresponding fracture energy.

The factors A^j_f and A^j_{mi} in Eqs.(32) and (33) adopt the form:

$$A^j_f = \frac{2L_c(R^j_\parallel)^2}{2E_\parallel \mathcal{G}^j_\parallel - L_c(R^j_\parallel)^2} \quad j = t,c \tag{34}$$

$$A^j_{m1} = \frac{2L_c(R^j_\perp)^2}{2E_\perp \mathcal{G}^j_\perp - L_c(R^j_\perp)^2}; \quad A^j_{m2} = \frac{2L_c(R_{\perp\parallel})^2}{2G_{\perp\parallel}\mathcal{G}_{\perp\parallel} - L_c(R_{\perp\parallel})^2} \qquad j = t,c \tag{35}$$

where $\mathcal{G}^t_\parallel$ and $\mathcal{G}^c_\parallel$ are the fracture energy in tension and in compression in fiber direction, respectively; $\mathcal{G}^t_\perp$ and $\mathcal{G}^c_\perp$ are the fracture energy in tension and in compression transverse to the fiber, respectively; $\mathcal{G}_{\perp\parallel}$ is the in-plane shear fracture energy; L_c is the characteristic length of the element to reduce the mesh dependency pathology through the so-called crack-band technique [5]. This strategy has been widely exploited by different authors, assuming different procedures for the computation of the characteristic element length [13, 38, 44].

For a given mesh size, the minimum values for the different fracture energies are:

$$\mathcal{G}^j_\parallel \geq \frac{L_c(R^j_\parallel)^2}{2E_\parallel}; \quad \mathcal{G}^j_\perp \geq \frac{L_c(R^j_\perp)^2}{2E_\perp}; \quad \mathcal{G}_{\perp\parallel} \geq \frac{L_c(R_{\perp\parallel})^2}{2G_{\perp\parallel}} \qquad j = t,c \tag{36}$$

Consequently, the conditions given in Eq.(36) determine the lowest possible value for these fracture energies at the onset of damage. Note that if the stored strain energy is equal to the fracture energy, the material would abruptly fails. This modeling approach is usually denominated as ply-discount technique [76]. Furthermore, if the fracture energy is chosen to be lower than the strain energy at the damage onset, the material fails before the failure criterion is ever satisfied. This leads to unrealistic physical responses, which exhibit local snap-back evolution after failure initiation in the corresponding stress-strain evolution.

3. Solid shell formulation

3.1. Kinematics

The solid shell parametrization of the shell kinematics has attracted an increasing interest in the research community due to its ability to overcome the well-known problems associated with the parametrization of

rotational degrees of freedom in finite strain analyses [3, 4, 32, 35, 57, 60, 66, 77]. According to such an approach, the kinematics of the deformation is described by using a linear interpolation of a pair of position vectors located at the top and bottom surfaces of the shell. The present solid shell formulation is based on the fundamental derivations developed by the authors in [61, 62, 63], whereby the element performance has been thoroughly examined under different loading conditions. In the current investigation, the main modifications of such solid shell formulation affect the interpolation scheme with regard to incompatible strains and the incorporation of the anisotropic continuum damage model herein proposed.

Exploiting this concept, the initial (undeformed) configuration of the shell body can be described by (Figure 3.a):

$$\mathbf{X}(\xi^1,\xi^2,\xi^3) = \frac{1}{2}\left[1+\xi^3\right]\mathbf{X}_t(\xi^1,\xi^2) + \frac{1}{2}\left[1-\xi^3\right]\mathbf{X}_b(\xi^1,\xi^2), \tag{37}$$

where $\mathbf{X}(\xi^1,\xi^2,\xi^3)$ is the material point in the reference configuration ($\mathbf{X}(\xi^1,\xi^2,\xi^3) \in \mathcal{B}_0$), which is expressed in terms of the top $\mathbf{X}_t(\xi^1,\xi^2)$ and bottom $\mathbf{X}_b(\xi^1,\xi^2)$ position vectors. These vectors are functions of the material coordinates $\boldsymbol{\xi} = \{\xi^1,\xi^2,\xi^3\}$, which represent the parametric curvilinear coordinates $\xi^i \in [-1,1]$ with $i = 1,2,3$. Thus, the top and bottom material points are identified with $\xi^3 = +1$ and $\xi^3 = -1$, respectively.

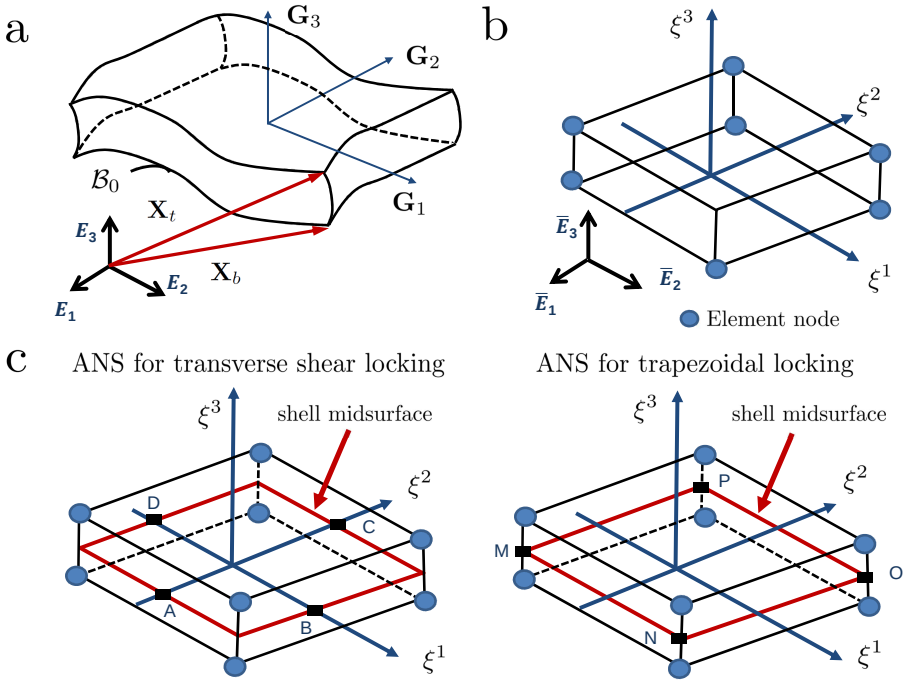

Figure 3: Solid shell formulation. (a) Parametrization of the reference configuration. (b) Kinematic discretization. (c) Collocation points for the use of the ANS method in order to alleviate transverse shear and trapezoidal locking pathologies.

Similarly, the parametrization of the current (deformed) configuration of the shell body reads:

$$\mathbf{x}(\xi^1,\xi^2,\xi^3) = \frac{1}{2}\left[1+\xi^3\right]\mathbf{x}_t(\xi^1,\xi^2) + \frac{1}{2}\left[1-\xi^3\right]\mathbf{x}_b(\xi^1,\xi^2), \tag{38}$$

where $\mathbf{x}(\xi^1,\xi^2,\xi^3)$ denotes an arbitrary point in the current configuration ($\mathbf{x}(\xi^1,\xi^2,\xi^3) \in \mathcal{B}_t$), whilst $\mathbf{x}_t(\xi^1,\xi^2)$ and $\mathbf{x}_b(\xi^1,\xi^2)$ denote the top and bottom position vectors, respectively.

The reference and current configurations are related via the displacement field:

$$\mathbf{x}(\boldsymbol{\xi}) = \mathbf{X}(\boldsymbol{\xi}) + \mathbf{u}(\boldsymbol{\xi}). \tag{39}$$

The curvilinear basis vectors in the reference, $\mathbf{G}_i$, and current, $\mathbf{g}_i$, configurations are given by:

$$\mathbf{G}_i = \frac{\partial \mathbf{X}(\boldsymbol{\xi})}{\partial \xi^i}; \quad \mathbf{g}_i = \frac{\partial \mathbf{x}(\boldsymbol{\xi})}{\partial \xi^i} = \mathbf{G}_i + \frac{\partial \mathbf{u}(\boldsymbol{\xi})}{\partial \xi^i} \quad i = 1, 2, 3 \tag{40}$$

The contravariant basis vectors in the reference and in the current configurations comply with the following relationships: $\mathbf{G}_i \cdot \mathbf{G}^j = \delta_i^j$ and $\mathbf{g}_i \cdot \mathbf{g}^j = \delta_i^j$, where δ_i^j is the Kronecker delta. The metric coefficients read: $g_{ij} = \mathbf{g}_i \cdot \mathbf{g}_j$ and $G_{ij} = \mathbf{G}_i \cdot \mathbf{G}_j$.

The compatible deformation gradient is defined as:

$$\mathbf{F}^u := \frac{\partial \mathbf{x}}{\partial \mathbf{X}} = \mathbf{g}_i \otimes \mathbf{G}^i. \tag{41}$$

The definition of the displacement compatible Green-Lagrange strain tensor reads:

$$\hat{\mathbf{E}}^u := \frac{1}{2}\left[(\mathbf{F}^u)^{\mathrm{T}} \mathbf{F}^u - \mathbb{I}_2 \right] = \frac{1}{2}\left[g_{ij} - G_{ij} \right] \mathbf{G}^i \otimes \mathbf{G}^j, \tag{42}$$

where $\mathbb{I}_2$ is the material metric tensor.

3.2. Variational basis

The variational basis of the Enhanced Assumed Strain (EAS) method relies on the mixed Hu-Washizu variational principle [68]. In the current solid shell formulation, the displacement-derived strain field, Eq.(42), is additively enhanced via an incompatible strain field, $\tilde{\mathbf{E}}$ [10]: $\hat{\mathbf{E}} = \hat{\mathbf{E}}^u + \tilde{\mathbf{E}}$.

In the total Lagrangian version, the variational formulation corresponding to the EAS method considers the displacement field, $\mathbf{u}$, the incompatible strain tensor, $\tilde{\mathbf{E}}$, and the second Piola-Kirchhoff stress tensor (energetically conjugated to $\hat{\mathbf{E}}$), $\mathbf{S}$, as independent variables. Through the adoption of the orthogonality condition between the parametrization spaces of the stress and enhancing strains, the stress field can be removed from the formulation [10, 35]. Correspondingly, the variation of the Hu-Washizu functional can be expressed as:

$$\delta\Pi(\mathbf{u}, \delta\mathbf{u}, \tilde{\mathbf{E}}, \delta\tilde{\mathbf{E}}) = \int_{\mathcal{B}_0} \mathbf{S} : \delta\hat{\mathbf{E}}^u \, \mathrm{d}\Omega + \int_{\mathcal{B}_0} \mathbf{S} : \delta\tilde{\mathbf{E}} \, \mathrm{d}\Omega - \delta\Pi_{\mathrm{ext}} = \delta\Pi_{\mathrm{int}} - \delta\Pi_{\mathrm{ext}}, \tag{43}$$

where $\delta\Pi_{\mathrm{int}}$ and $\delta\Pi_{\mathrm{ext}}$ respectively identify the internal and external contributions to the functional. The stress field can be expressed as a function of the strain field, i.e. $\mathbf{S} = \mathbf{S}(\hat{\mathbf{E}}) := \partial\Psi/\partial\hat{\mathbf{E}} = \partial_{\hat{\mathbf{E}}}\Psi(\hat{\mathbf{E}})$, where $\Psi(\hat{\mathbf{E}})$ identifies the Helmholtz free-energy function, Eq.(2).

3.3. Finite element formulation

3.3.1. Kinematic interpolation

According to the isoparametric concept, the interpolation of the reference and current configurations is performed using the standard trilinear shape functions (Figure 3.b):

$$\mathbf{X} \approx \sum_{A=1}^{8} N^A(\boldsymbol{\xi}) \mathbf{X}_A = \mathbf{N}\mathbf{X}^e; \quad \mathbf{x} \approx \sum_{A=1}^{8} N^A(\boldsymbol{\xi}) \mathbf{x}_A = \mathbf{N}\mathbf{x}^e, \tag{44}$$

where $N^A(\boldsymbol{\xi})$ are the standard shape functions, $\mathbf{X}_A$ and $\mathbf{x}_A$ account for the nodal position points in the reference and current configurations, respectively; $\mathbf{N}$ identifies the matrix collecting the standard element shape functions, and $\mathbf{X}^e$ and $\mathbf{x}^e$ denote the operators that arrange the nodal position vectors in the reference and current configurations, respectively.

The interpolation of the displacement field, its variation ($\delta\mathbf{u}$) and its increment ($\Delta\mathbf{u}$) can be expressed as

$$\mathbf{u} \approx \sum_{A=1}^{8} N^A \mathbf{d}_A = \mathbf{N}\mathbf{d}; \; \delta\mathbf{u} \approx \sum_{A=1}^{8} N^A \delta\mathbf{d}_A = \mathbf{N}\delta\mathbf{d}; \; \Delta\mathbf{u} \approx \sum_{A=1}^{8} N^A \Delta\mathbf{d}_A = \mathbf{N}\Delta\mathbf{d}, \tag{45}$$

where $\mathbf{d}$ identify the vector of nodal displacements.

The variation and increment of the compatible strain field can be interpolated according to the following scheme:

$$\delta\hat{\mathbf{E}}^u \approx \mathbf{B}(\mathbf{d})\delta\mathbf{d}, \quad \Delta\hat{\mathbf{E}}^u \approx \mathbf{B}(\mathbf{d})\Delta\mathbf{d}, \tag{46}$$

where $\mathbf{B}(\mathbf{d})$ stands for the displacement-strain operator.

3.3.2. Assumed Natural Strain (ANS) method

The ANS method is herewith considered with the aim of tackling transverse shear [6] and trapezoidal [8] locking effects. This numerical technique has been widely employed in different shell and solid shell models [10, 32, 35, 61].

Within the Lagrangean setting, transverse shear locking is remedied by modifying the interpolation of the transverse shear strain components $\hat{E}_{13}$ and $\hat{E}_{23}$ [6]:

$$\begin{bmatrix} 2\hat{E}_{13}^{ANS} \\ 2\hat{E}_{23}^{ANS} \end{bmatrix} = \begin{bmatrix} (1-\xi^2)2\hat{E}_{13}(\boldsymbol{\xi}_A) + (1+\xi^2)2\hat{E}_{13}(\boldsymbol{\xi}_C) \\ (1+\xi^1)2\hat{E}_{23}(\boldsymbol{\xi}_B) + (1-\xi^1)2\hat{E}_{23}(\boldsymbol{\xi}_D) \end{bmatrix} \rightarrow \begin{bmatrix} \hat{E}_{\parallel\perp} \\ \hat{E}_{\perp\perp} \end{bmatrix}. \tag{47}$$

The coordinates of the collocation points in this strategy in the parametric element space are the following: $\boldsymbol{\xi}_A = (0,-1,0)$, $\boldsymbol{\xi}_B = (1,0,0)$, $\boldsymbol{\xi}_C = (0,1,0)$ and $\boldsymbol{\xi}_D = (-1,0,0)$, see Figure 3.c.

In bending dominated applications, locking effects can emerge due to artificial transverse normal strains, especially in formulations which perform a direct interpolation of the director vector [10]. To alleviate such locking pathology (usually denominated as trapezoidal locking), a similar modification of the interpolation scheme of the transverse normal strain component $\hat{E}_{33}$ as that outlined in Eq.(47) can be accomplished. In particular, the interpolation proposed in [8, 10] is herewith assumed, which reads:

$$\begin{aligned} \hat{E}_{33}^{ANS} &= \sum_{m=1}^{4} N^m(\xi^1,\xi^2)\hat{E}_{33} \rightarrow \hat{E}_{\perp\perp}, \quad m = M,N,O,P \\ N^m(\xi^1,\xi^2) &= \frac{1}{4}\left(1+\xi_m^1\xi^1\right)\left(1+\xi_m^2\xi^2\right), \quad \text{with } \xi_m^1,\xi_m^2 = \pm 1 \end{aligned} \tag{48}$$

The collocation points given in Eq.(48) are placed at the corner points of the shell midsurface (Figure 3.c): $\boldsymbol{\xi}_M = (-1,-1,0)$, $\boldsymbol{\xi}_N = (1,-1,0)$, $\boldsymbol{\xi}_O = (1,1,0)$ and $\boldsymbol{\xi}_P = (-1,1,0)$.

Finally, it is worth mentioning that the modification of the interpolation of the transverse shear strain components according to the ANS method introduces changes in the computation of the $\mathbf{B}$-operator and the geometrical stiffness matrix, as addressed in [60].

3.3.3. Interpolation of the incompatible strains

The so-called membrane, Poisson thickness and volumetric locking pathologies is alleviated by means of the EAS technique [10, 68]. In particular, as described above, the additive decomposition of the Green-Lagrange strain tensor is here adopted [10], whereby the enhanced part is interpolated at the element level according to the form:

$$\tilde{\mathbf{E}} \approx \mathbf{M}(\boldsymbol{\xi})\boldsymbol{\varsigma}, \tag{49}$$

where $\boldsymbol{\varsigma}$ is the vector of the independent parameters (incompatible strain components) and $\mathbf{M}(\boldsymbol{\xi})$ is the interpolation operator in the global Cartesian setting. As was discussed in [35], it is usual to define an interpolation matrix $\tilde{\mathbf{M}}$, which is defined in the local parametric space and requires a subsequent transformation into the global space of analysis.

Similarly, the variation ($\delta\tilde{\mathbf{E}}$) and the increment ($\Delta\tilde{\mathbf{E}}$) of the incompatible strains are interpolated as follows:

$$\delta\tilde{\mathbf{E}} \approx \mathbf{M}(\boldsymbol{\xi})\delta\boldsymbol{\varsigma}, \quad \Delta\tilde{\mathbf{E}} \approx \mathbf{M}(\boldsymbol{\xi})\Delta\boldsymbol{\varsigma}. \tag{50}$$

In the current investigation, a combination of the enhancing schemes proposed in [77, 57] leading to 15 EAS parameters is furnished. This EAS design allows the locking deficiencies mentioned above to be tackled. The interpolation of the incompatible strains in the parametric space reads:

$$\tilde{\mathbf{M}}(\boldsymbol{\xi}) = \begin{bmatrix} \xi^1 & \xi^1\xi^2 & \xi^1\xi^3 & 0 & 0 & 0 & 0 & 0 & 0 & 0 & 0 & 0 & 0 & 0 & 0 \\ 0 & 0 & 0 & \xi^1 & \xi^2 & \xi^1\xi^3 & \xi^2\xi^3 & 0 & 0 & 0 & 0 & 0 & 0 & 0 & 0 \\ 0 & 0 & 0 & 0 & 0 & 0 & 0 & 0 & 0 & 0 & 0 & 0 & 0 & 0 & 0 \\ 0 & 0 & 0 & 0 & 0 & 0 & 0 & \xi^2 & \xi^1\xi^2 & \xi^2\xi^3 & 0 & 0 & 0 & 0 & 0 \\ 0 & 0 & 0 & 0 & 0 & 0 & 0 & 0 & 0 & 0 & 0 & 0 & 0 & 0 & 0 \\ 0 & 0 & 0 & 0 & 0 & 0 & 0 & 0 & 0 & 0 & \xi^1 & \xi^2 & \xi^1\xi^2 & \xi^1\xi^3 & \xi^2\xi^3 \end{bmatrix} \tag{51}$$

Introducing the discretization schemes corresponding to the kinematic and the incompatible strain fields presented above and performing the consistent linearization of the residual equations, the following resulting systems of equations at element level can be obtained:

$$\begin{bmatrix} \mathbf{k}_{dd} & \mathbf{k}_{d\varsigma} \\ \mathbf{k}_{\varsigma d} & \mathbf{k}_{\varsigma\varsigma} \end{bmatrix} \begin{bmatrix} \Delta\mathbf{d} \\ \Delta\boldsymbol{\varsigma} \end{bmatrix} = \begin{bmatrix} \mathbf{f}_{\text{ext}} \\ 0 \end{bmatrix} - \begin{bmatrix} \mathbf{f}_{\text{int}} \\ \mathbf{f}_{\text{EAS}} \end{bmatrix} \tag{52}$$

The internal force vectors $\mathbf{f}_{\text{int}}$ and $\mathbf{f}_{\text{EAS}}$ are given by:

$$\mathbf{f}_{\text{int}} = \int_{\mathcal{B}_0} \mathbf{B}^{\text{T}}\mathbf{S}\ \text{d}\Omega; \quad \mathbf{f}_{\text{EAS}} = \int_{\mathcal{B}_0} \mathbf{M}^{\text{T}}\mathbf{S}\ \text{d}\Omega. \tag{53}$$

The element stiffness matrices $\mathbf{k}_{dd}$, $\mathbf{k}_{d\varsigma}$, $\mathbf{k}_{\varsigma d}$ and $\mathbf{k}_{\varsigma\varsigma}$ are defined as:

$$\mathbf{k}_{dd} = \int_{\mathcal{B}_0} \left(\mathbf{B}^{\text{T}}\tilde{\mathbb{C}}\mathbf{B} + \left(\frac{\partial \mathbf{B}}{\partial \mathbf{d}}\right)^{\text{T}} \mathbf{S} \right) \text{d}\Omega; \quad \mathbf{k}_{d\varsigma} = \int_{\mathcal{B}_0} \mathbf{B}^{\text{T}}\tilde{\mathbb{C}}\mathbf{M}\ \text{d}\Omega \tag{54}$$

$$\mathbf{k}_{\varsigma d} = \int_{\mathcal{B}_0} \mathbf{M}^{\text{T}}\tilde{\mathbb{C}}\mathbf{B}\ \text{d}\Omega; \qquad \mathbf{k}_{\varsigma\varsigma} = \int_{\mathcal{B}_0} \mathbf{M}^{\text{T}}\tilde{\mathbb{C}}\mathbf{M}\ \text{d}\Omega, \tag{55}$$

where $\tilde{\mathbb{C}}$ represents the Lagrangean tangent material tensor.

Note that the enhanced strains can be condensed out from the final system due to the fact that these parameters are interpolated discontinuously across the element boundaries. Therefore, the current formulation preserves the size of the standard displacement shell model.

3.4. Intralaminar damage formulation in geometrically nonlinear regime

The anisotropic damage model herewith proposed (Section 2) can be accordingly formulated within the finite strain framework by means of expressing the Helmholtz free energy definition, Eq.(2), in terms of the corresponding energetically conjugated pairs. Thus, for a Lagrangian description, which fulfills the restriction stating that the undeformed state is stress-free, the energy function can be written using the Green-Lagrange strain tensor, $\hat{\mathbf{E}}$, and the second Piola-Kirchhoff stress tensor, $\mathbf{S}$, as energetic counterparts:

$$\mathbf{S} := \partial_{\hat{\mathbf{E}}}\Psi(\hat{\mathbf{E}}, \tilde{\mathfrak{d}}); \qquad \tilde{\mathbb{C}} := \partial^2_{\hat{\mathbf{E}}\hat{\mathbf{E}}}\Psi(\hat{\mathbf{E}}, \tilde{\mathfrak{d}}). \tag{56}$$

The use of a general nonlinear formulation allows the incorporation of geometric effects into the current modeling strategy to be performed. Consequently, the current preferential orientation $\mathbf{a}$ can be computed from the mapping of the reference material orientation, $\mathbf{a}_0$, via the deformation gradient:

$$\mathbf{a} = \mathbf{F}\mathbf{a}_0 \tag{57}$$

However, the use of EAS method to prevent locking pathologies requires the computation of the total deformation gradient $\mathbf{F}$, which accounts for the displacement derived, $\mathbf{F}^u$, and a modified counterpart, $\tilde{\mathbf{F}}$. This tensor can be determined by means of the exploitation of the total Cauchy–Green tensor [32, 61]:

$$\mathbf{C} := \mathbf{C}^u + \tilde{\mathbf{C}} = 2(\hat{\mathbf{E}}^u + \tilde{\mathbf{E}}) + \mathbb{I}_2. \tag{58}$$

A final ingredient that should be taken into consideration is the fact that the tangent tensor derived in Section 2 is referred to the current configuration. In order to keep the consistency with the current solid shell formulation, such operator should be referred to the Lagrangian configuration by means of standard pull-back operations [33].

4. Computational procedure: finite element implementation

This section outlines the main aspects of the FE implementation of the damage model herein envisaged. The proposed model is implemented into the commercial FE package ABAQUS through the user-defined subroutine `UMAT`. This routine is called at each material integration point at the element level at each time increment. The nonlinear solution procedure is based on the standard incremental-iterative Newton-Raphson process, where the Cauchy nominal stress tensor, the consistent tangent operator and the internal variables that characterize the damage development should be updated at each pseudo-time increment.

4.1. Derivation of the consistent tangent operator

The achievement of quadratic convergence along the solution process requires the computation of the consistent tangent operator, which can be expressed as $\mathbb{C}^{tg} = \frac{\partial \boldsymbol{\sigma}}{\partial \boldsymbol{\varepsilon}}$. Recalling the stress definition given in Eq.(9), the damage tangent operator reads:

$$\mathbb{C}^{tg} = \frac{\partial \boldsymbol{\sigma}}{\partial \boldsymbol{\varepsilon}} = \sum_i (1-\mathfrak{d}_{it})(1-\mathfrak{d}_{ic})\mathbb{C}_i^e - \sum_i (1-\mathfrak{d}_{ic})\frac{\partial \mathfrak{d}_{it}}{\partial \boldsymbol{\varepsilon}} \otimes \bar{\boldsymbol{\sigma}}_i - \sum_i (1-\mathfrak{d}_{it})\frac{\partial \mathfrak{d}_{ic}}{\partial \boldsymbol{\varepsilon}} \otimes \bar{\boldsymbol{\sigma}}_i \quad i = f, m1, m2. \tag{59}$$

The resultant spatial tangent operator is generally nonsymmetric. The first term of the tangent operator is usually identified as the secant operator $\mathbb{C}^{sec}$, see Eq.(13), which takes the form:

$$\mathbb{C}^{sec} = \frac{\partial \boldsymbol{\sigma}}{\partial \boldsymbol{\varepsilon}} = \sum_i (1-\mathfrak{d}_{it})(1-\mathfrak{d}_{ic})\bar{\mathbb{C}}_i^e \quad i = f, m1, m2. \tag{60}$$

Particularizing Eq.(59) to the present model renders:

$$\begin{aligned} \mathbb{C}^{tg} = \mathbb{C}^{sec} &- (1-\mathfrak{d}_{fc})\frac{\partial f_{ft}}{\partial \boldsymbol{\varepsilon}} \otimes \bar{\boldsymbol{\sigma}}_f - (1-\mathfrak{d}_{ft})\frac{\partial f_{fc}}{\partial \boldsymbol{\varepsilon}} \otimes \bar{\boldsymbol{\sigma}}_f - (1-\mathfrak{d}_{m1c})\frac{\partial f_{m1t}}{\partial \boldsymbol{\varepsilon}} \otimes \bar{\boldsymbol{\sigma}}_{m1} \\ &- (1-\mathfrak{d}_{m1t})\frac{\partial f_{m1c}}{\partial \boldsymbol{\varepsilon}} \otimes \bar{\boldsymbol{\sigma}}_{m1} - (1-\mathfrak{d}_{m2c})\frac{\partial f_{m2t}}{\partial \boldsymbol{\varepsilon}} \otimes \bar{\boldsymbol{\sigma}}_{m2} - (1-\mathfrak{d}_{m2t})\frac{\partial f_{m2c}}{\partial \boldsymbol{\varepsilon}} \otimes \bar{\boldsymbol{\sigma}}_{m2}. \end{aligned} \tag{61}$$

The derivatives of the damage variables with respect to the strain tensor can be defined by applying the chain rule as follows:

$$\begin{aligned} &\frac{\partial f_{ft}}{\partial \boldsymbol{\varepsilon}} = \frac{\partial f_{ft}}{\partial f_{E,FF+}}\left(\frac{\partial f_{E,FF+}}{\partial \bar{\boldsymbol{\sigma}}} : \frac{\partial \bar{\boldsymbol{\sigma}}}{\partial \boldsymbol{\varepsilon}}\right); \qquad \frac{\partial f_{fc}}{\partial \boldsymbol{\varepsilon}} = \frac{\partial f_{fc}}{\partial f_{E,FF-}}\left(\frac{\partial f_{E,FF-}}{\partial \bar{\boldsymbol{\sigma}}} : \frac{\partial \bar{\boldsymbol{\sigma}}}{\partial \boldsymbol{\varepsilon}}\right); \\ &\frac{\partial f_{m1t}}{\partial \boldsymbol{\varepsilon}} = \frac{\partial f_{m1t}}{\partial f_{E,IFF+}}\left(\frac{\partial f_{E,IFF+}}{\partial \bar{\boldsymbol{\sigma}}} : \frac{\partial \bar{\boldsymbol{\sigma}}}{\partial \boldsymbol{\varepsilon}}\right); \quad \frac{\partial f_{m1c}}{\partial \boldsymbol{\varepsilon}} = \frac{\partial f_{m1c}}{\partial f_{E,IFF-}}\left(\frac{\partial f_{E,IFF-}}{\partial \bar{\boldsymbol{\sigma}}} : \frac{\partial \bar{\boldsymbol{\sigma}}}{\partial \boldsymbol{\varepsilon}}\right); \\ &\frac{\partial f_{m2t}}{\partial \boldsymbol{\varepsilon}} = \frac{\partial f_{m2t}}{\partial f_{E,IFF+}}\left(\frac{\partial f_{E,IFF+}}{\partial \bar{\boldsymbol{\sigma}}} : \frac{\partial \bar{\boldsymbol{\sigma}}}{\partial \boldsymbol{\varepsilon}}\right); \quad \frac{\partial f_{m2c}}{\partial \boldsymbol{\varepsilon}} = \frac{\partial f_{m2c}}{\partial f_{E,IFF-}}\left(\frac{\partial f_{E,IFF-}}{\partial \bar{\boldsymbol{\sigma}}} : \frac{\partial \bar{\boldsymbol{\sigma}}}{\partial \boldsymbol{\varepsilon}}\right), \end{aligned} \tag{62}$$

where the variation of the damage variables with respect to the exposure factors is given by

$$\begin{aligned} &\frac{\partial f_{fj}}{\partial f_{E,FF}} = \frac{1}{f_{E,FF}^2}\left(1 + A_f^j f_{E,FF}\right)\left(A_f^j(1-f_{E,FF})\right) \quad j = t, c; \\ &\frac{\partial f_{mij}}{\partial f_{E,IFF}} = \frac{1}{f_{E,IFF}^2}\left(1 + A_{mi}^j f_{E,IFF}\right)\left(A_{mi}^j(1-f_{E,IFF})\right) \quad i = 1, 2; \quad j = t, c. \end{aligned} \tag{63}$$

The components of the derivatives of the tangent tensor are detailed in Appendix A.

4.2. Viscous regularization

Implicit FE computations attaining stiffness degradation are often interrupted due to convergence problems in achieving equilibrium conditions. To circumvent this numerical issue, a viscous regularization of the damage state variables can be accomplished [43, 44]. For a particular damage variable $\mathfrak{d}_j$, this regularization procedure can be expressed as:

$$\dot{\mathfrak{d}}_j^v = \frac{1}{\eta}\left[\mathfrak{d}_j - \mathfrak{d}_j^v\right] \quad \text{with} \quad j = \{ft, fc, m1t, m1c, m2t, m2c\}. \tag{64}$$

In Eq.(64) $\dot{d}_j^v$ is the rate of the viscous damage variable, $\mathfrak{d}_j^v$ is the viscous damage variable and η stands for the viscosity parameter. Within the time increment $[t_n, t_{n+1}]$ along the solution process, the viscous damage variable at the state t_{n+1}, i.e. $\mathfrak{d}_{j,n+1}^v$ can be computed as the weighted average of the damage variable at the current time increment $\mathfrak{d}_{j,n+1}$, weighted by the load increment ($\Delta t = t_{n+1} - t_n$) and the regularized damage variable at the previous increment $\mathfrak{d}_{j,n}^v$ weighted by the viscosity parameter. The final expression of the current viscous damage variable renders:

$$\mathfrak{d}_{j,n+1}^v = \frac{\Delta t}{\eta + \Delta t}\mathfrak{d}_{j,n+1} + \frac{\eta}{\eta + \Delta t}\mathfrak{d}_{j,n}^v \tag{65}$$

4.3. Implementation algorithm

In this section, the numerical algorithmic treatment of the proposed nonlinear material model is outlined. Particularizing the procedure for a pseudo-time increment $\left[t_n, t_{n+1}^{(k)}\right]$ along the loading history, for a given iteration k (in the following magnitudes referred to this iteration are denoted by the superscript k), the numerical algorithm consists of an initial elastic predictor that is used to evaluate the damage criterion, and the subsequent computation of the internal variables at the current state in case of damage growth.

The fracture plane is determined through the evaluation of the IFF Eqs.(21) and (22) from $[-90°, 90°]$ with an angle increment of $0.1°$. The present model also encompasses the hypothesis stating that once inter-fiber damage is predicted to take place at any material integration point, the orientation of the fracture plane θ_{fp} is assumed to be constant for posterior loading increments. Therefore, the search for the fracture plane is not necessarily to be computed again.

4.3.1. Puck material model: `UMAT` description

This section describes the computational procured regarding the implementation of the Puck-based constitutive model (Section 2) via the used-defined capability `UMAT` of ABAQUS.

Relying on a strain driven procedure, the set of given variables at the beginning of the increment are $\{\Delta\boldsymbol{\varepsilon}_{n+1}^{(k)}, \boldsymbol{\varepsilon}_n, \boldsymbol{\sigma}_n, \tilde{\mathfrak{d}}_n, \mathbf{r}_n\}$, where $\Delta\boldsymbol{\varepsilon}_{n+1}^{(k)}$ identifies the strain increment, $\boldsymbol{\varepsilon}_n$ and $\boldsymbol{\sigma}_n$ stand for the previous converged strain and stress fields, respectively, and $\tilde{\mathfrak{d}}_n$ and $\mathbf{r}_n$ are the vectors damage variables and damage thresholds at the time step t_n with $j = \{ft, fc, m1t, m1c, m2t, m2c\}$. Note that the damage variables and the damage thresholds are internal variables, which are considered within the context of ABAQUS as state-dependent variables (`SDV`). With these data, the updated set of variables that the user should provide is $\{\boldsymbol{\sigma}_{n+1}^{(k)}, \mathbb{C}_{n+1}^{tg(k)}, \tilde{\mathfrak{d}}_{n+1}^{(k)}, \mathbf{r}_{n+1}^{(k)}\}$. Algorithm 1 details the computational procedure for the FE implementation of the present model.

4.3.2. Solid shell FE model: `UEL` description

This sections outlines the implementation algorithm of the previous constitutive damage model into the solid shell FE formulation (Section 3) using the subroutine `UEL`. This procedure follows the main guidelines thoroughly discussed by the authors in [60]. The current implementation relies on the use of the state dependent variables (`SDVs`) for the treatment of the incompatible strains along the nonlinear procedure. These `SDVs` are stored in the array `SVARS` of ABAQUS.

Since the size and meaning of such variables are defined by the user, in this case, with the aim of simplifying the implementation, the array `SVARS` contains at integration point level: (i) the enhancing

Given $\{\Delta\boldsymbol{\varepsilon}_{n+1}^{(k)}, \boldsymbol{\varepsilon}_n, \boldsymbol{\sigma}_n, \tilde{\mathfrak{d}}_n, \mathbf{r}_n\}$ the initial data at the iteration k between the interval $\left[t_n, t_{n+1}^{(k)}\right]$

1. Update the strain tensor $\boldsymbol{\varepsilon}_{n+1}^{(k)} = \boldsymbol{\varepsilon}_n + \Delta\boldsymbol{\varepsilon}_{n+1}^{(k)}$;
2. Construct the operators: $\mathbb{C}_f^e$, $\mathbb{C}_{m1}^e$, $\mathbb{C}_{m2}^e$;
3. Compute the effective stress tensor (elastic predictor): $\bar{\boldsymbol{\sigma}}_{n+1}^{(k)} = \sum_i \mathbb{C}_i^e : \boldsymbol{\varepsilon}_{n+1}^{(k)}$ with $i = f, m1, m2$;
4. Using the effective stress, perform the computation of the exposure factors $f_{E,FF+,n+1}^{(k)}(\bar{\boldsymbol{\sigma}}_{n+1}^{(k)})$, $f_{E,FF-,n+1}^{(k)}(\bar{\boldsymbol{\sigma}}_{n+1}^{(k)})$, $f_{E,IFF+,n+1}^{(k)}(\bar{\boldsymbol{\sigma}}_{n+1}^{(k)})$, $f_{E,IFF-,n+1}^{(k)}(\bar{\boldsymbol{\sigma}}_{n+1}^{(k)})$;
5. Check the fiber-failure criterion Eq.(30);
   if $\bar{\boldsymbol{\sigma}}_{11,n+1}^{(k)} \geq 0$ **then**
   Calculate $r_{E,FF+,n+1}^{(k)}$, $\mathfrak{d}_{ft,n+1}^{(k)}$ Eq.(32);
   else
   Calculate $r_{E,FF-,n+1}^{(k)}$, $\mathfrak{d}_{fc,n+1}^{(k)}$ Eq.(32);
   end
6. Check inter-fiber-failure criterion Eq.(30);
   if $r_{E,IFF+,n} == 1 \parallel r_{E,IFF+,n} == 1$ **then**
   Search for the fracture plane $\theta_{fp,n+1}^{(k)}$;
   Compute $\bar{\sigma}_{n,n+1}^{(k)}(\theta)$, $\bar{\tau}_{nt,n+1}^{(k)}(\theta)$, $\bar{\tau}_{n1,n+1}^{(k)}(\theta)$ Eq.(19);
   Calculate the strength value $R_{\perp\psi}^A$ Eq.(25);
   Compute $p_{\perp\psi}^t$ and $p_{\perp\psi}^c$ Eq.(24);
   end
   if $\bar{\boldsymbol{\sigma}}_{n,n+1}^{(k)} \geq 0$ **then**
   Calculate $r_{E,IFF+,n+1}^{(k)}$, $\mathfrak{d}_{m1t,n+1}^{(k)}$, $\mathfrak{d}_{m2t,n+1}^{(k)}$ Eq.(33);
   else
   Calculate $r_{E,IFF-,n+1}^{(k)}$, $\mathfrak{d}_{m1c,n+1}^{(k)}$, $\mathfrak{d}_{m2c,n+1}^{(k)}$;
   end
   In case of damage onset, set $\theta_{fp} \leftarrow \theta_{fp,n+1}^{(k)}$
7. Update the state dependent variables $\tilde{\mathfrak{d}}_{n+1}^{(k)}, \mathbf{r}_{n+1}^{(k)}$;
8. Compute secant operator $\mathbb{C}_{n+1}^{sec(k)}$ Eq.(60);
9. Calculate the stress tensor $\boldsymbol{\sigma}$ Eq.(9);
10. Compute tangent operator $\mathbb{C}_{n+1}^{tg(k)}$ Eq.(61);

Algorithm 1: FE implementation of the consistent anisotropic damage model based on the Puck criterion.

strains at element level (15 `SDVs`), (ii) the stress and strain components (12 `SDVs`), (iii) the material tangent operator (36 `SDVs`) and (iv) the damage variables previously defined along with the fracture angle (7 `SDVs`).

The computation of the enhancing strains update at element level is performed via examining the second row of the system given in Eq.(52). Thus, the increment of the enhancing strains at a given iteration can be determined through the following expression:

$$\Delta\boldsymbol{\varsigma}_n^{(k)} = -\left[\mathbf{k}_{\varsigma\varsigma,n}\right]^{-1}\left[\mathbf{f}_{\mathrm{EAS},n} + \mathbf{k}_{\varsigma d,n}\Delta\mathbf{d}^{(k)}\right]. \tag{66}$$

Note that the exploitation of the scheme given in Eq.(66) requires the inversion of the matrices $\mathbf{k}_{\varsigma\varsigma,n}$ and $\mathbf{k}_{\varsigma\varsigma,n+1}^{(k)}$ (which are square matrices whose size is coincident with the number of EAS parameters) at

each time step along the solution process. In addition to the previous considerations, the integration of the Puck-based model into the solid shell element requires the use of standard pull-back and push-forward operations in order to express the constitutive tangent operator into the material setting. These operations are omitted here for the sake of brevity, see [33]. Algorithm 2 drafts the main steps for the current numerical process.

Given $\{\mathbf{d}_n, \boldsymbol{\varsigma}_n, \Delta\mathbf{d}_{n+1}^{(k)}\}$ and $\{\tilde{\mathfrak{d}}_n, \mathbf{r}_n\}$ the initial data at the iteration k between the interval $\left[t_n, t_{n+1}^{(k)}\right]$

1. Update the tentative nodal displacements $\mathbf{d}_{n+1}^{(k)} = \mathbf{d}_n + \Delta\mathbf{d}_{n+1}^{(k)}$
2. Perform at integration point level on the shell midsurface at configuration t_n
   (a) Construct the B-operator $\mathbf{B}_n$
   (b) Modify the metric interpolation due to ANS method
   (c) Perform loop over the material layers
      i. Computation of the curvilinear basis $\mathbf{g}_{i,n}$, $\mathbf{G}_{i,n}$
      ii. Determine Deformation Gradient $\mathbf{F}_n$
      iii. Compute push-forward operations
      iv. Compute constitutive block Algorithm 1
      v. Perform the numerical integration of the constitutive law over the thickness
   (d) Compute pull-back operations to obtain $\mathbf{S}_n$ and $\tilde{\mathbb{C}}_n$
   (e) Compute the operators: $\mathbf{k}_{\varsigma d,n}$, $\mathbf{k}_{\varsigma\varsigma,n}$, $\mathbf{f}_{\text{int},n}$ and $\mathbf{f}_{\text{EAS},n}$
   (f) Compute $\Delta\boldsymbol{\varsigma}_n^{(k)} = -\left[\mathbf{k}_{\varsigma\varsigma,n}\right]^{-1}\left[\mathbf{f}_{\text{EAS},n} + \mathbf{k}_{\varsigma d,n}\Delta\mathbf{d}^{(k)}\right]$
   (g) Update the enhancing strains $\boldsymbol{\varsigma}_{n+1}^{(k)} = \boldsymbol{\varsigma}_n + \Delta\boldsymbol{\varsigma}_n^{(k)}$
3. Perform at integration point level on the shell midsurface at configuration $t_{n+1}^{(k)}$
   (a) Construct the B-operator $\mathbf{B}_{n+1}^{(k)}$
   (b) Modify the metric interpolation due to ANS method
   (c) Perform loop over the material layers
      i. Computation of the curvilinear basis $\mathbf{g}_{i,n+1}^{(k)}$, $\mathbf{G}_{i,n+1}^{(k)}$
      ii. Compute the enhancing strains $\tilde{\mathbf{E}}_{n+1}^{(k)} = \mathbf{M}\boldsymbol{\varsigma}_{n+1}^{(k)}$
      iii. Determine Deformation Gradient $\mathbf{F}_n$
      iv. Compute constitutive block Algorithm 1
      v. Perform the numerical integration of the constitutive law over the thickness
4. Compute pull-back operations to obtain $\mathbf{S}_n$ and $\tilde{\mathbb{C}}_n$
5. Compute the operators $\mathbf{k}_{dd,n+1}^{(k)}$, $\mathbf{k}_{\varsigma d,n+1}^{(k)}$, $\mathbf{k}_{d\varsigma,n+1}^{(k)}$ $\mathbf{k}_{\varsigma\varsigma,n+1}^{(k)}$, $\mathbf{f}_{\text{int},n+1}^{(k)}$ and $\mathbf{f}_{\text{EAS},n+1}^{(k)}$
6. Perform the static condensation of $\boldsymbol{\varsigma}_{n+1}^{(k)}$ and construct $\tilde{\mathbf{k}}_{dd,n+1}^{(k)}$ and $\tilde{\mathbf{f}}_{\text{int},n+1}^{(k)}$
7. Solve for the new displacement increment $\tilde{\mathbf{k}}_{dd,n+1}^{(k)}\Delta\mathbf{d}_{n+1}^{(k)} = \mathbf{f}_{\text{ext}} - \tilde{\mathbf{f}}_{\text{int},n+1}^{(k)}$

Algorithm 2: FE implementation of the Puck-based damage model into the solid shell element.

5. Applications

This section is concerned with the assessment of the proposed anisotropic Puck-based damage model for layered composites (Section 2, and its integration into the solid shell element outlined in Section 3 by means of several applications. The current constitutive model and the solid shell formulation have been implemented into the FE package ABAQUS through the procedure described in Section 4.

5.1. Cyclic loading and mesh sensitivity assessment: benchmark examples

The first example under consideration assesses the performance of the current damage model under cyclic tensile–compressive loading. The defined boundary conditions are: (i) fully clamped nodes at the side $\mathbf{e}_1 = 0$, and (ii) prescribed displacements $\bar{u}$ at the side $\mathbf{e}_1 = L$, with side length $L = 1$ mm, see Figure 5. The chosen material properties are listed in Tables 3–5, which replicate those outlined in [26, 27]. The simulations are performed using both approaches here addressed: (1) a single 8-node element C3D8 of ABAQUS incorporating the developed damage model via the `UMAT` capability (Section 4.3.1), and (2) a solid shell element which includes the corresponding damage material model into the `UEL` implementation. Both capabilities provide identical results.

First, the model consists of a single element under a prescribed compressive displacement $\bar{u}$ transverse to the fibre direction. Figure 4 shows the absolute stress-strain evolution curve (transverse to the fiber direction), where an exponential degradation once the criterion is violated can be observed. The orientation of the fracture plane is stored as state dependent variable (Figure 4). Thus, under such uniaxial compressive conditions, this angle is predicted to be around $\theta_{fp} = 53^\circ \pm 2^\circ$, which is in line with the Puck theory (Section 2.2) and with the experimental observations in [21, 22].

Load step	Prescribed displacement $\bar{u}$ [mm]
1	0.007
2	0.000
3	-0.020
4	0.000
5	0.007
6	0.020

Table 2: Loading sequence for cycling benchmark application.

E_{11} (GPa)	E_{22}, E_{33} (GPa)	G_{12} (GPa)	G_{13} (GPa)	ν_{12}, ν_{13}
139.7	12.9	6.9	6.9	0.23

Table 3: Material properties for T300/976 [27].

$R_{\parallel}^{t}{}^{*}$ (MPa)	$R_{\parallel}^{c}{}^{*}$ (MPa)	$R_{\perp}^{t}{}^{*}$ (MPa)	$R_{\perp}^{c}{}^{*}$ (MPa)	$R_{\parallel\perp}{}^{*}$ (MPa)
1516.8	1592.7	44.54	253	106.8

Table 4: Strength properties for T300/976 [27].* Labelling of the strength parameters. Longitudinal tensile strength $R_{\parallel}^{t}$; longitudinal compressive strength $R_{\parallel}^{c}$; transverse tensile strength $R_{\perp}^{t}$; transverse compressive strength $R_{\perp}^{c}$; in-plane shear strength $R_{\parallel\perp}$.

$\mathcal{G}_{\parallel}^{t}$ (N/mm)	$\mathcal{G}_{\parallel}^{c}$ (N/mm)	$\mathcal{G}_{\perp}^{t}$ (N/mm)	$\mathcal{G}_{\perp}^{c}$ (N/mm)	$\mathcal{G}_{\parallel\perp}^{t}$ (N/mm)
91.6	79.9	0.22	0.76	0.46

Table 5: Fracture energies for T300/976 [27].

Subsequently, the cube is subjected to the loading conditions according to the sequence reported in Table 2 (transverse to the fibre direction). Figure 5 shows the reaction force–displacement evolution for the current benchmark application, where it can be seen that the provoked damage along the tensile part of the cycle is accounted for in the following compressive evolution. Indeed, the further damage propagation in this latter stage generates a corresponding stiffness degradation through the evolution of the compressive damage variable $\mathfrak{d}_{m1c}$. This effect can be appreciated in the subsequent tensile part of the application.

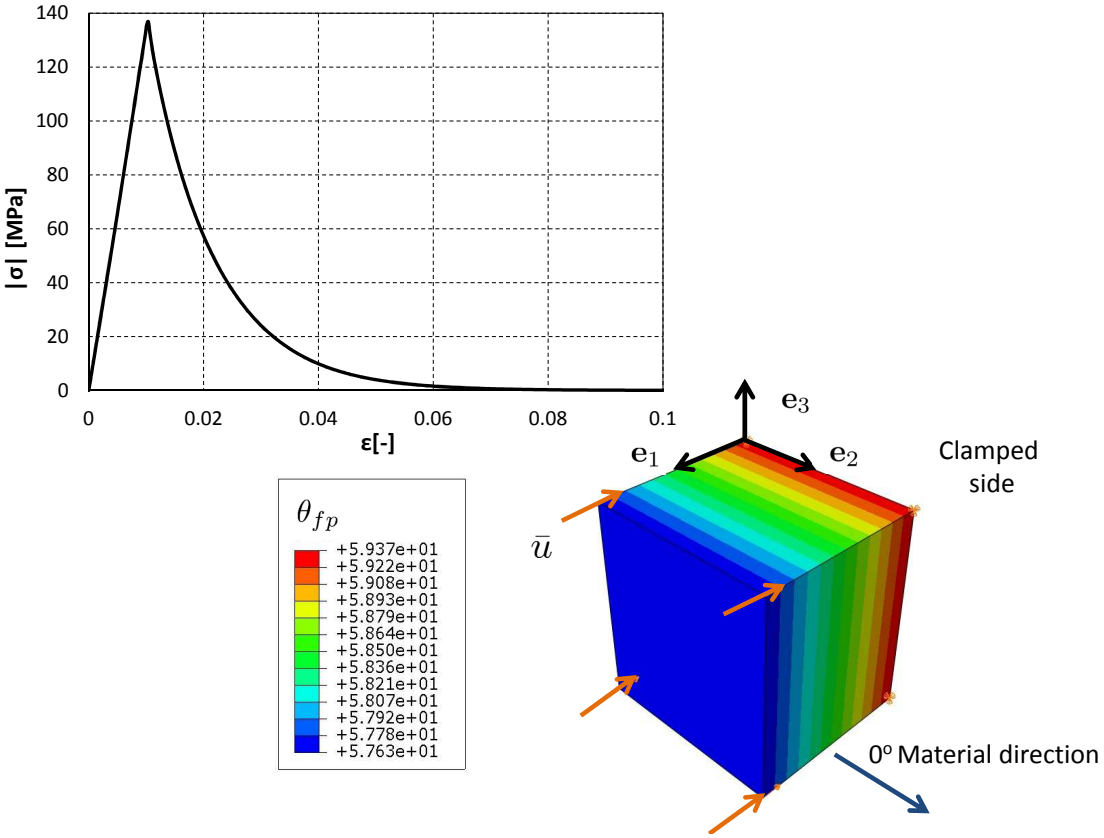

Figure 4: Transverse stress-strain evolution curve under uniaxial compressive state and estimation of the failure angle.

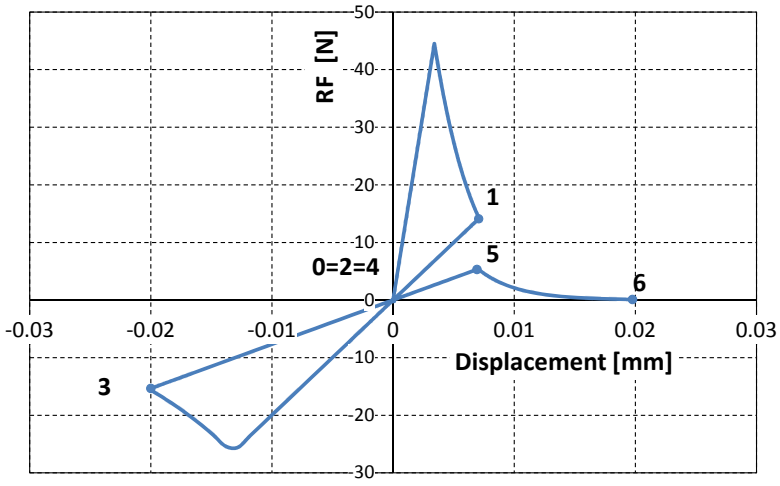

Figure 5: Load–displacement curves under uniaxial tensile-compressive cycling load.

The second benchmark application is concerned with the analysis of the mesh sensitivity of the developed model. This mesh dependency analysis is performed by means of evaluating the effectiveness of the crack

band approach to remedy strain localization pathologies [38, 43]. Herewith, we reproduce the analysis conducted in [27], which consists of testing a cube with four different meshes. The side length is equal to 1 mm, which is meshed using 1 element, 9 elements, 125 elements and 343 elements. A single element of the block placed at its centre is defined with a slightly lower strength (10% lower than those given in Table 4) in order to promote damage initiation at this location. The prescribed tensile displacement is set equal to 0.05 mm transverse to the fibre direction, whilst the supporting conditions and the material orientation are defined coincident with those corresponding to the previous cycling example.

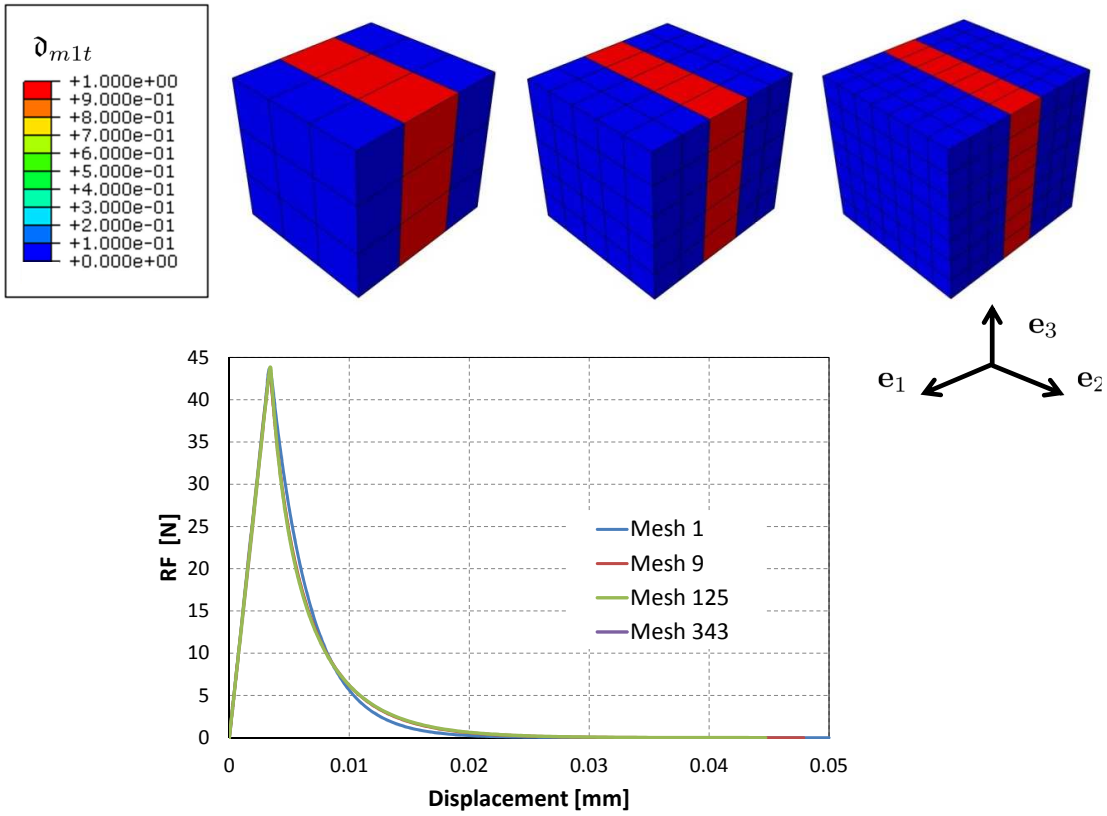

Figure 6: Load–displacement curves under uniaxial tensile loading for different mesh refinements. Estimation of tensile fiber failure.

Figure 6 shows the tensile matrix failure prediction using the proposed computational framework, which, as expected, is smeared over a band of one element in width. This estimation is fully consistent with that discussed in [27]. Examining the load displacement evolution curve (Figure 6), it can be seen that the use of the crack band approach leads to very close evolutions independent of the mesh density. Indeed, this is a very effective strategy, especially for elements with aspect ratios equal or close to 1 with respect to the in-plane and out-of-plane dimensions [38].

5.2. Open hole tension test

The proposed damage formulation is applied to simulate the progressive failure analysis of open-hole fibre reinforced specimen. Different studies analyzing the mechanical performance and size effects of open-hole composite components have been carried from experimental and numerical standpoints using different methods, see [13, 19, 18].

The geometric definition of the specimen under consideration is shown in Figure 7, replicating that previously investigated in [13], and whose main dimensions are: axial length $L = 100$ mm, width $w = 12$

mm, thickness $t = 3$ mm, hole diameter $d = 2$ mm. The laminates are manufactured from IM7-8552 CFRP, whose mechanical properties are reported in Tables 6-8. The reference material orientation is aligned with the longitudinal direction of the specimen, which coincides with the loading direction. The laminate disposal corresponds to the following quasi-isotropic arrangement: $[90/0/\pm 45]_{3S}$.

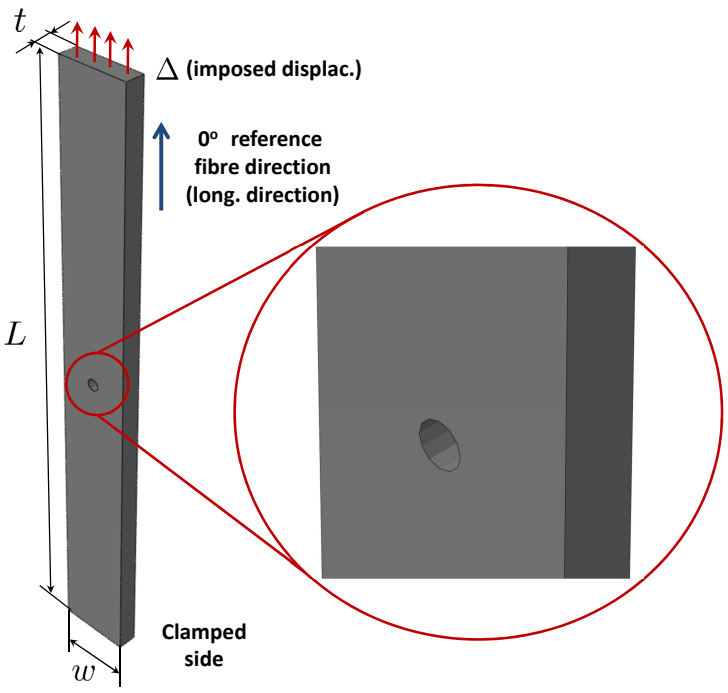

Figure 7: Open hole specimen: geometric definition.

E_{11} (GPa)	E_{22}, E_{33} (GPa)	G_{12} (GPa)	G_{13} (GPa)	ν_{12}, ν_{13}
171.42	9.08	5.39	5.39	0.32

Table 6: Material properties for IM7-8552 [13].

$R^t_{\parallel}$ (MPa)	$R^c_{\parallel}$ (MPa)	$R^t_{\perp}$ (MPa)	$R^c_{\perp}$ (MPa)	$R_{\parallel\perp}$ (MPa)
2323.5	1200.1	62.3	199.8	92.3

Table 7: Strength properties for IM7-8552 [13]. Labelling of the strength parameters: longitudinal tensile strength $R^t_{\parallel}$, longitudinal compressive strength $R^c_{\parallel}$, transverse tensile strength $R^t_{\perp}$, transverse compressive strength $R^c_{\perp}$, in-plane shear strength $R_{\parallel\perp}$.

$\mathcal{G}^t_{\parallel}$ (N/mm)	$\mathcal{G}^c_{\parallel}$ (N/mm)	$\mathcal{G}^t_{\perp}$ (N/mm)	$\mathcal{G}^c_{\perp}$ (N/mm)	$\mathcal{G}^t_{\parallel\perp}$ (N/mm)
81.5	106.3	0.2774	1.3092	0.7879

Table 8: Fracture energies for IM7-8552 [43, 44].

In the experimental program, four different specimens complying with the previous definition are tested in a MTS servo-hydraulic machine according to the ASTM D-5766 standard [78] under monotonic tensile

loading along the axial direction. The average remote failure stress measured during the tests is equal to 555.7 MPa, with a standard deviation of 15.33 MPa. The first ply failure that is identified during the experiments corresponds to matrix breakage of the outer layer (with an orientation of 90° with respect to the loading direction). Figure 8 depicts one of the specimens after the test, where the failure mode corresponds to net-section tension [13]. The specimens are visually inspected after the experimental program, observing a combination of intralaminar and interlaminar damage events.

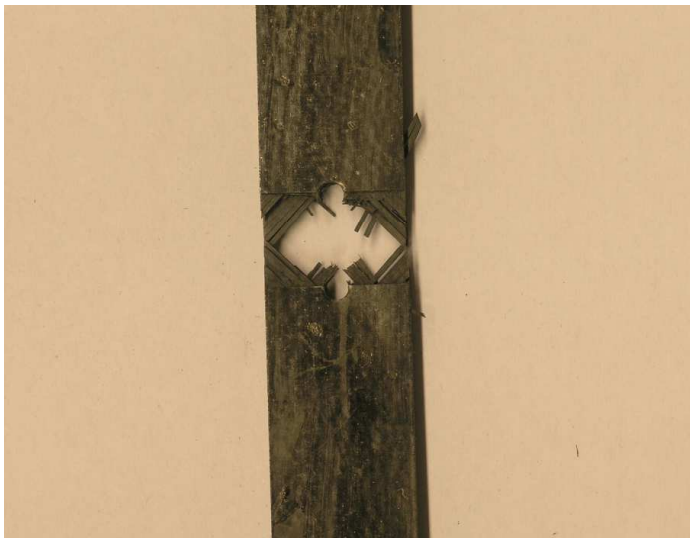

Figure 8: Open hole specimen: failure evidences after the test.

With regard to the numerical analysis, several models with the geometric definition described above are discretized using one layer of the solid shell element for each of the plies of the laminate (this discretization can be interpreted as a layer-wise (LW) approach). These elements are equipped with the proposed 3D anisotropic damage model to account for intralaminar damage (note that also models including the user-defined capability `UMAT` are also created, leading to similar estimations). It is worth noting that differing from previous investigations [13, 19, 18], the current modeling framework allows computing 3D stress state at ply level.

In situ-strengths are also incorporated into the analysis using the formulation proposed in [12], which are functions of the fracture toughness and the elastic properties. Based on this procedure, the following in-situ strengths are calculated: (i) $R_{\perp}^{t} = 106.2$ MPa for a thin embedded ply and $R_{\perp}^{t} = 101.4$ MPa for a thin outer ply, and (ii) $R_{\parallel\perp} = 130.2$ MPa for a thin embedded ply and $R_{\parallel\perp} = 107.0$ MPa for a thin outer ply. The shear strength in the transverse direction in computed according to the following expression:

$$R_{\perp\perp} = R_{\perp}^{c} \cos\theta_{fp} \left[\sin\theta_{fp} + \frac{\cos\theta_{fp}}{\tan 2\theta_{fp}} \right]. \tag{67}$$

Then, for a fracture angle $\theta_{fp} = 53°$, the transverse shear strength results: $R_{\perp\perp} = 75.3$ MPa.

In order to account for the interaction of intralaminar and interlaminar damage events within the simulations, one layer of cohesive interface elements are inserted between the plies in order to trigger interlaminar failure. Particularly, the built-in cohesive formulation of ABAQUS, which relies on the formulation outlined in [11], is used obeying a bilinear traction separation law (TSL). The interface properties here considered are listed in Table 9. The interface failure for mixed fracture conditions is attained using the 3D version of the Benzeggah-Kenane (BK) failure criterion [7]:

$$\mathcal{G}_c = \mathcal{G}_{Ic} + (\mathcal{G}_{IIc} - \mathcal{G}_{Ic}) \left(\frac{\mathcal{G}_{II} + \mathcal{G}_{III}}{\mathcal{G}_I + \mathcal{G}_{II} + \mathcal{G}_{III}} \right)^{\eta}, \tag{68}$$

where $\mathcal{G}_c$ is the fracture toughness for mixed fracture conditions; $\mathcal{G}_{Ic}$ and $\mathcal{G}_{IIc}$ represent fracture toughness for Modes I and II, respectively; $\mathcal{G}_I$, $\mathcal{G}_{II}$ and $\mathcal{G}_{III}$ stand for the energy release rates for Modes I, II and III, respectively.

σ^c (MPa)	τ^c (MPa)	$\mathcal{G}_{IC}$ (J/m2)	$\mathcal{G}_{IIC}$ (J/m2)	η
33.5141	56.2941	280	790	1.45

Table 9: Interlaminar fracture properties for IM7/8552. σ^c and τ^c denote the critical normal and shear tractions for softening initiation; $\mathcal{G}_{IC}$ and $\mathcal{G}_{IIC}$ stand for the Mode I and II fracture toughness, respectively (assuming $\mathcal{G}_{IC} = \mathcal{G}_{IIIC}$); η identifies the BK fitting exponent.

Preliminary simulations are conducted in order to assess the numerical results with respect to the mesh size, leading to the following discretization: (i) 115296 solid shell elements, and (ii) 110492 `COH3D8` cohesive elements of ABAQUS. Note that using such element topologies, conforming meshes in terms of density and kinematic displacements interpolation are employed. Simulations are performed using 1000 pseudo-time step increments under displacement control using an implicit nonlinear FE scheme with a non-symmetric solver. The ultimate average stress from the computations is 541.22 MPa, slightly underestimating the experimental measure with a deviation equal to 2.61 %. Regarding the solution procedure, notable numerical difficulties in achieving equilibrium solutions are observed at very advanced loading stages (beyond 90% of the ultimate load) at which different nonlinearities stemming from the used damage capabilities are developed. Therefore, in order to achieve complete the computation, artificial viscous damping using the `*stabilize` option of ABAQUS is employed.

Figure 9 shows numerical-experimental correlation corresponding to the reaction force-displacement evolution curve. In this graph, a bilinear characteristic response is observed where two stages can be identified: (i) an initial linear evolution where no damage events are predicted to take place, and (ii) a subsequent quasi-linear stage characterized by the development of intralaminar and interlaminar failure. The current model accurately captures this response though slight deviations with regard to the specimen stiffness can be observed.

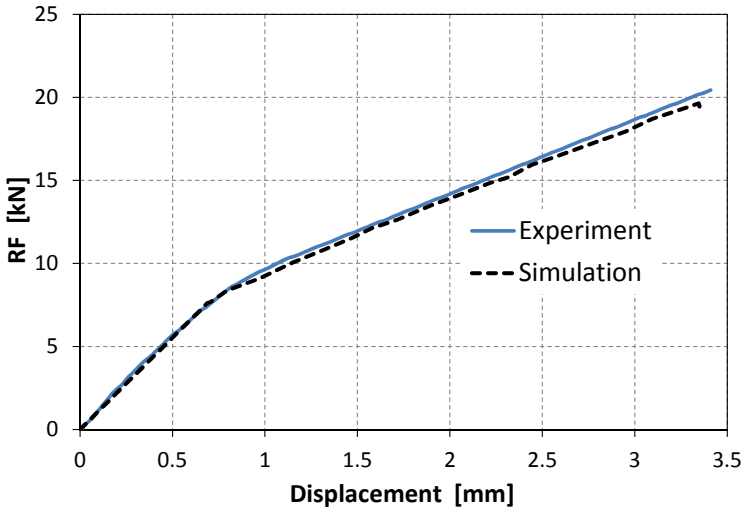

Figure 9: Load–displacement curve for the open hole specimen: experimental-numerical correlation.

Intralaminar failure pattern predictions corresponding to tensile matrix and fibre damage variables using the proposed methodology are shown in Figure 10 for different loading states. The outer 90° ply exhibits a characteristic X-shaped matrix tensile-failure crack pattern. The onset of this damage event is predicted to occur at around 32% of the numerically estimated ultimate load. The crack pattern of the top 0° ply

is characterized by tensile fiber failure. This failure mode is initially concentrated around the hole and subsequently it propagates perpendicular to the loading direction. This leads to the estimation of net-section failure mode, which causes the failure of the specimen. This estimation is in line with the failure mode observed during the experimental program. Regarding interlaminar damage, Figure 11, the current computations predict the initiation and growth of delamination events (in red are depicted delaminated areas) at different interfaces, especially severe delamination events are observed at the 0/45 interfaces, being in good agreement with the predictions presented in [19] for similar open hole configurations. In this graph, delamination events are predicted to be developed more concentrated around the hole area for the 90/0 interfaces, featuring a different pattern in comparison with the 0/45 interfaces.

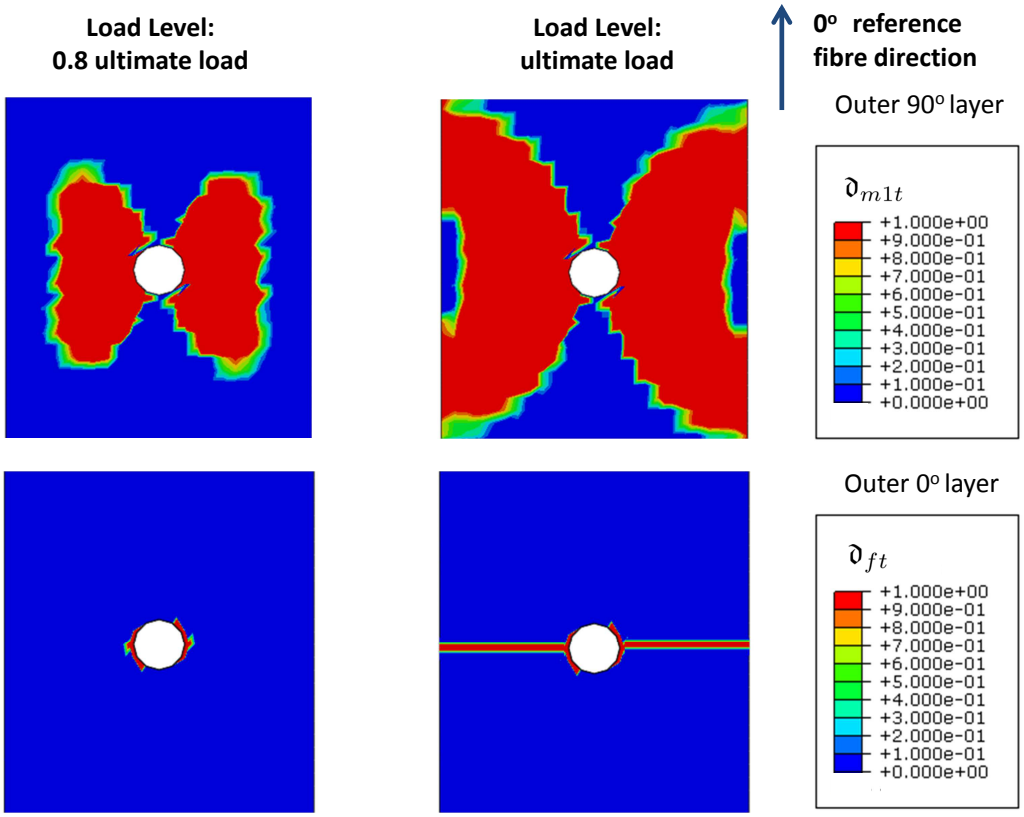

Figure 10: Intralamaninar failure patterns for the open hole specimen: tensile matrix and fiber damage variables at different load levels.

6. Conclusions

In this investigation, a novel three-dimensional anisotropic damage model for fibre reinforced composites has been developed. The 3D Puck failure theory was used to predict intralaminar failure onset (first ply damage), whereas failure growth has been derived by means of satisfying the thermodynamic restrictions in terms of the Clausius-Plank inequality under isothermal conditions.

The inelastic response relied on the definition of six damage variables (considering damage propagation under tensile and compressive stress states), which accounted for distinction between two intralaminar failure mechanisms at ply level: (i) fibre failure (FF), and (ii) inter-fibre failure (IFF). The effect of ply thickness was also taken into consideration by means of using the so-called in-situ strength properties in the 3D Puck failure theory according with the formulation proposed in [12].

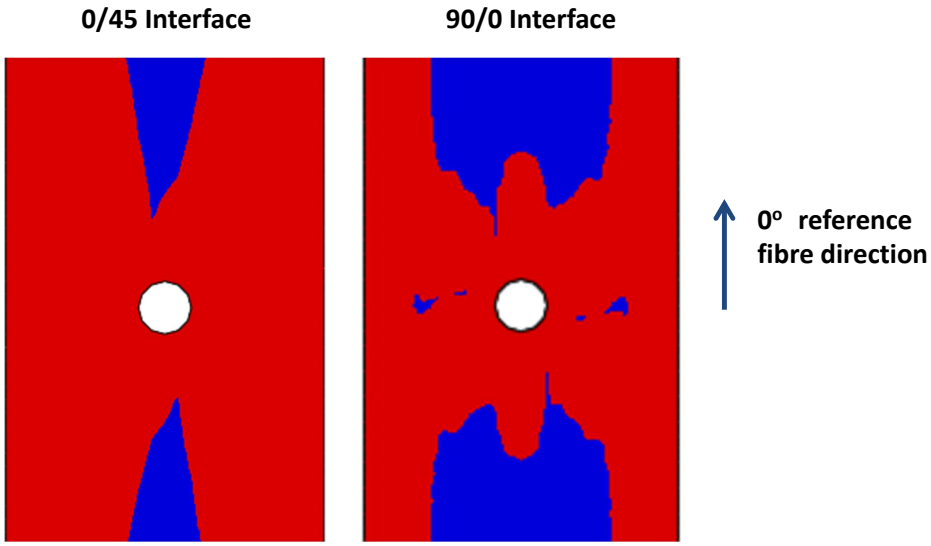

Figure 11: Interlaminar failure patterns for the open hole specimen at the ultimate load: delaminated and intact regions are represented in red and blue, respectively.

From the computational standpoint, specific details with regard to the numerical implementation of the current formulation into the user-defined capabilities of ABAQUS `UMAT` and `UEL` has been addressed. In particular, the `UEL`-version (user-defined element) employed a locking-free solid shell element, which allowed the use of 3D constitutive models in efficient shell-based computations. In addition, a central aspect of the proposed modeling technique is the fact that it was constructed within the framework of general nonlinear setting, therefore geometrically nonlinear effects can be incorporated into the analysis.

The proposed computational model was verified by means of two benchmark problems. The first benchmark application showed the performance under uniaxial compressive loading and tensile-compressive cycling loading both transverse to the fiber direction, whereas the second verification example assessed the alleviation of the mesh sensitivity through the crack band approach. Finally, the current formulation was validated by means of an structural example which consisted of an open hole tension specimen. This latter application illustrated the applicability of the current numerical approach to account for the interaction of intralaminar and interlaminar (interface cohesive elements) modelling tools for accurate damage analysis in structural components.

Acknowledgments

JR and AB are grateful to the support of the Andalusian Government (Projects of Excellence P11-TEP-7093 and P12-TEP-1050) and the Spanish Ministry of Economy and Competitiveness (DPI2012-37187, MAT2015-71036-P and MAT2015-71309-P). PPC author gratefully acknowledges the funding of Project NORTE-01-0145-FEDER-000022 SciTech Science and Technology for Competitive and Sustainable Industries, co-financed by Programa Operacional Regional do Norte (NORTE2020), Fundo Europeu de Desenvolvimento Regional (FEDER).

Appendix A. Derivatives of the tangent operator

The terms needed to compute the tangent operator can be expressed as

$$\begin{aligned}
\frac{\partial f_{E,FF\pm}}{\partial \varepsilon_{11}} &= \frac{1}{R_{\parallel}^{t,c}}\left[\mathbb{C}_{11}^{e} - \left(\nu_{\perp\parallel} - \frac{E_{\parallel}}{E_{\parallel f}}\right)\left(\mathbb{C}_{21}^{e} + \mathbb{C}_{31}^{e}\right)\right] \\
\frac{\partial f_{E,FF\pm}}{\partial \varepsilon_{22}} &= \frac{1}{R_{\parallel}^{t,c}}\left[\mathbb{C}_{12}^{e} - \left(\nu_{\perp\parallel} - \frac{E_{\parallel}}{E_{\parallel f}}\right)\left(\mathbb{C}_{22}^{e} + \mathbb{C}_{32}^{e}\right)\right] \\
\frac{\partial f_{E,FF\pm}}{\partial \varepsilon_{33}} &= \frac{1}{R_{\parallel}^{t,c}}\left[\mathbb{C}_{13}^{e} - \left(\nu_{\perp\parallel} - \frac{E_{\parallel}}{E_{\parallel f}}\right)\left(\mathbb{C}_{23}^{e} + \mathbb{C}_{33}^{e}\right)\right] \\
\frac{\partial f_{E,FF\pm}}{\partial \varepsilon_{12}} &= 0 \\
\frac{\partial f_{E,FF\pm}}{\partial \varepsilon_{13}} &= 0 \\
\frac{\partial f_{E,FF\pm}}{\partial \varepsilon_{23}} &= 0
\end{aligned} \tag{A.1}$$

With respect to the derivatives corresponding to inter-fibre failure, a more complicated procedure has to be performed. The term $f_{E,IFF\pm}$ for tension and compression can be expressed as

$$f_{E,IFF\pm} = \sqrt{\mathcal{A}\bar{\sigma}_n^2(\theta_{fp}) + \mathcal{B}\bar{\tau}_{nt}^2(\theta_{fp}) + \mathcal{C}\bar{\tau}_{n1}^2(\theta_{fp})} + \mathcal{D}\bar{\sigma}_n(\theta_{fp}), \tag{A.2}$$

where $\mathcal{A}$, $\mathcal{B}$, $\mathcal{C}$ and $\mathcal{D}$ are material parameters. We also denote $c = \cos\theta_{fp}$ and $s = \sin\theta_{fp}$ to simplify the notation. Making use of the previous definitions, the local stress components acting on the failure plane take the form

$$\begin{aligned}
\bar{\sigma}_n(\theta_{fp}) &= \varepsilon_{11}\left(\mathbb{C}_{21}^{e}c^2 + \mathbb{C}_{31}^{e}s^2\right) + \varepsilon_{22}\left(\mathbb{C}_{22}^{e}c^2 + \mathbb{C}_{32}^{e}s^2\right) + \varepsilon_{33}\left(\mathbb{C}_{23}^{e}c^2 + \mathbb{C}_{33}^{e}s^2\right) + \gamma_{23}2cs\mathbb{C}_{66}^{e} \\
\bar{\tau}_{nt}(\theta_{fp}) &= \varepsilon_{11}\left(-\mathbb{C}_{21}^{e}sc + \mathbb{C}_{31}^{e}sc\right) + \varepsilon_{22}\left(-\mathbb{C}_{22}^{e}sc + \mathbb{C}_{32}^{e}sc\right) + \varepsilon_{33}\left(-\mathbb{C}_{23}^{e}sc + \mathbb{C}_{33}^{e}sc\right) + \gamma_{23}\left(c^2 - s^2\right)\mathbb{C}_{66}^{e} \\
\bar{\tau}_{n1}(\theta_{fp}) &= \gamma_{31}s\mathbb{C}_{55}^{e} + \gamma_{21}s\mathbb{C}_{44}^{e},
\end{aligned} \tag{A.3}$$

with

$$\mathcal{R} = \mathcal{A}\bar{\sigma}_n^2(\theta_{fp}) + \mathcal{B}\bar{\tau}_{nt}^2(\theta_{fp}) + \mathcal{C}\bar{\tau}_{n1}^2(\theta_{fp}). \tag{A.4}$$

The final derivative terms read

$$\begin{aligned}
\frac{\partial f_{E,IFF\pm}}{\partial \varepsilon_{11}} &= \frac{1}{2\sqrt{\mathcal{R}}}\left[2\mathcal{A}\left(\mathbb{C}_{21}^{e}c^2 + \mathbb{C}_{31}^{e}s^2\right)\bar{\sigma}_n + 2\mathcal{B}\left(-\mathbb{C}_{21}^{e}sc + \mathbb{C}_{31}^{e}sc\right)\bar{\tau}_{nt}\right] + \mathcal{D}\left(\mathbb{C}_{21}^{e}c^2 + \mathbb{C}_{31}^{e}s^2\right) \\
\frac{\partial f_{E,IFF\pm}}{\partial \varepsilon_{22}} &= \frac{1}{2\sqrt{\mathcal{R}}}\left[2\mathcal{A}\left(\mathbb{C}_{22}^{e}c^2 + \mathbb{C}_{32}^{e}s^2\right)\bar{\sigma}_n + 2\mathcal{B}\left(-\mathbb{C}_{22}^{e}sc + \mathbb{C}_{32}^{e}sc\right)\bar{\tau}_{nt}\right] + \mathcal{D}\left(\mathbb{C}_{22}^{e}c^2 + \mathbb{C}_{32}^{e}s^2\right) \\
\frac{\partial f_{E,IFF\pm}}{\partial \varepsilon_{33}} &= \frac{1}{2\sqrt{\mathcal{R}}}\left[2\mathcal{A}\left(\mathbb{C}_{23}^{e}c^2 + \mathbb{C}_{33}^{e}s^2\right)\bar{\sigma}_n + 2\mathcal{B}\left(-\mathbb{C}_{23}^{e}sc + \mathbb{C}_{33}^{e}sc\right)\bar{\tau}_{nt}\right] + \mathcal{D}\left(\mathbb{C}_{23}^{e}c^2 + \mathbb{C}_{33}^{e}s^2\right) \\
\frac{\partial f_{E,IFF\pm}}{\partial \varepsilon_{12}} &= \frac{1}{\sqrt{\mathcal{R}}}\left[2c\mathcal{C}\mathbb{C}_{44}^{e}\bar{\tau}_{n1}\right] \\
\frac{\partial f_{E,IFF\pm}}{\partial \varepsilon_{13}} &= \frac{1}{\sqrt{\mathcal{R}}}\left[2s\mathcal{C}\mathbb{C}_{55}^{e}\bar{\tau}_{n1}\right] \\
\frac{\partial f_{E,IFF\pm}}{\partial \varepsilon_{23}} &= \frac{1}{\sqrt{\mathcal{R}}}\left[4cs\mathcal{A}\mathbb{C}_{66}^{e}\bar{\sigma}_n + 2\left(c^2 - s^2\right)\mathcal{B}\mathbb{C}_{66}^{e}\bar{\tau}_{nt}\right] + 4cs\mathcal{D}\mathbb{C}_{66}^{e}
\end{aligned} \tag{A.5}$$

References

[1] Abaqus-Inc. Abaqus user manual, Version 6.9. Dassault Systems Simulia Corp, Providence, RI, USA; 2010.

[2] Abu Al-Rub, R.K., Voyiadjis, G.Z. (2003) On the coupling of anisotropic damage and plasticity models for ductile materials. International Journal of Solids and Structures, 40:2611–2643.

[3] Areias, P., Rabczuk, T., de Sá, J.C., Jorge, R.N. (2015) A semi-implicit finite strain shell algorithm using in-plane strains based on least-squares. Computational Mechanics 55(4):673–696.

[4] Areias, P., Rabczuk, T., Reinoso, J., César de Sá, J. (2016) Finite-strain low order shell using least-squares strains and two-parameter thickness extensibility. European Journal of Mechanics-A/Solids 61, 293–314.

[5] Bažant, Z., Oh, B.H. (1983) Crack band theory for fracture of concrete, Mat. Constr. 16(3):155–177.

[6] Bathe KJ, Dvorkin EN. (1985) A four-node plate bending element based on Mindlin/Reissner plate theory and a mixed interpolation. International Journal for Numerical Methods in Engineering, 21: 367-383.

[7] Benzeggagh ML, Kenane M. (1996) Measurement of mixed-mode delamination fracture toughness of unidirectional glass/epoxy composites with mixedmode bending apparatus. Comp Sci Tech 56(4):43949.

[8] Betsch P, Stein E. (1995) An assumed strain approach avoiding artificial thickness straining for a non-linear 4-node shell element. Commun. Numer. Methods Engng. 11:899-909.

[9] Blázquez A., Reinoso J., París F., Cañas J. (2012) Analysis in the postbuckling regime of a pressurized stiffened panel Part II: Numerical analysis and effect of the geometric imperfections. Compos Struct 94:1544–1554.

[10] Bischoff, M., Ramm, E. (1997) Shear Deformable Shell Elements for Large Strains and Rotations. International Journal for Numerical Methods in Engineering, 40:4427-4449.

[11] Camanho, P.P, Dávila, C.G., de Moura, M.F. (2003) Numerical simulation of mixed-mode progressive delamination in composite materials. J. Compos. Mater. 37, 1415–1438.

[12] Camanho, P.P., Dávila, C.G., Pinho, S.T., Iannucci, L., Robinson, P. (2006) Prediction of in-situ strengths and matrix cracking in composites under transverse tension and inplane shear. Composites: Part A 37:165176.

[13] Camanho, P.P., Maimí, P., Dávila, C.G. (2007) Prediction of size effects in notched laminates using continuum damage mechanics, Composites Science and Technology 67(13):2715–2727.

[14] Catalanotti, G., Camanho, P.P., Marques, A.T. (2013) Three-dimensional failure criteria for fiber-reinforced laminates, Compos Struct. 95:63–79.

[15] Catalanotti, G., Xavier, J., Camanho, P.P. (2014) Measurement of the compressive crack resistance curve of composites using the size effect law, Compos. Part A 56(0):300–307.

[16] Catalanotti, G., Arteiro, A., Hayati, M., Camanho, P.P. (2014) Determination of the mode I crack resistance curve of polymer composites using the size-effect law. Eng Fract Mech 118:49–65.

[17] Catalanotti, G., Xavier, J. (2015) Measurement of the mode II intralaminar fracture toughness and R-curve of polymer composites using a modified Iosipescu specimen and the size effect law, Eng. Fract. Mech. 138:202–214.

[18] Chen, J.F., Morozov, E.V., Shankar, K. (2014) Simulating progressive failure of composite laminates including in-ply and delamination damage effect. Compos Part A, 61:185–200.

[19] Chen, B.Y., Tay, T., Baiz, P., Pinho, S. (2013) Numerical analysis of size effects on open-hole tensile composite laminates. Composites: Part A, 47:52–62.

[20] Coleman, B.D, Noll, W. (1963) The thermodynamics of elastic materials with heat conduction and viscosity. Archive for Rational Mechanics and Analysis, 13:167-178.

[21] Correa , E., Mantič, V., París, F. (2008) Numerical characterisation of the fibrematrix interface crack growth in composites under transverse compression. Engineering Fracture Mechanics 75 (14), 4085–4103.

[22] Correa , E., Mantič, V., París, F. (2008) A micromechanical view of inter-fibre failure of composite materials under compression transverse to the fibres. Composites Science and Technology 68 (9), 2010–2021.

[23] Deuschle, H. M., Kröplin, B.-H (2012) Finite element implementation of Pucks failure theory for fibre-reinforced composites under three-dimensional stress. Journal of Composite Materials, 46:2485–2513.

[24] Deuschle, H. M., Puck, A. (2013) Application of the Puck Failure Theory for Fibre Reinforced Composites under 3D-Stress: Comparison with Experimental Results. Journal of Composite Materials, 47(6-7):827–846.

[25] Eliopoulos, E.N., Kostopoulos, V., Philippidis, T. P. (2016) A three-dimensional progressive damage FE model for GFRP composites under monotonic loading. Composites Science and Technology, 123:79–91.

[26] Falzon, B.G., Apruzzese, P. (2011) Numerical analysis of intralaminar failure mechanisms in composite structures. Part I: FE implementation. Compos Struct. 93(2):1039–1046.

[27] Falzon, B.G., Apruzzese, P. (2011) Numerical analysis of intralaminar failure mechanisms in composite structures. Part II: Applications. Compos Struct. 93(2):1047–1053.

[28] Frizzell, R.M., McCarthy, C.T., McCarthy, M.A. (2011) Simulating damage and delamination in fibre metal laminate joints using a three-dimensional damage model with cohesive elements and damage regularisation. Compos Sci Technol 2011;71(9):122535.

[29] Germain, N., Besson, J., Feyel, F. (2007) Composite layered materials: anisotropic nonlocal damage models. Comput Meth Appl Mech Eng 196(41–44): 4272–4282.

[30] Goyal, V. K.; Jaunky, N.; Johnson, E.; and Ambur, D. (2004) Intralaminar and Interlaminar Progressive Failure Analyses of Composite Panels with Circular Cutouts. Composite Structures, 64:91–105.

[31] Hashin, Z. (1980) Failure Criteria for Unidirectional Fiber Composites. Journal of Applied Mechanics, 47:329–334.

[32] Hauptmann, R., Schweizerhof, K. (1998) A systematic development of solid-shell element formulations for linear and non-linear analyses employing only displacement degrees of freedom. International Journal for Numerical Methods in Engineering 42:49–69.

[33] Holzapfel G. A. (2000) Nonlinear solid mechanics. John Wiley & Sons Ltd. ISBN: 978-0-471-82319-3.
[34] Kachanov, L. (1986) Introduction to Continuum Damage Mechanics. Martinus Nijhoff Publishers, Dordrecht, The Netherlands. ISBN: 978-94-017-1957-5.
[35] Klinkel, S., Wagner, W. (1997) A geometrical nonlinear brick element based on the easmethod. International Journal for Numerical Methods in Engineering 40: 4529–4545.
[36] Jirásek, M. (1998) Nonlocal models for damage and fracture: Comparison of approaches. Int. J. Solids Struct. 35:4133-4145.
[37] Ladeveze, P., LeDantec, E. (1992) Damage modeling of the elementary ply for laminated composites. Compos Sci Technol 43(3):257–267.
[38] Lapczyk, I., Hurtado, J.A. (2007) Progressive damage modeling in fiber-reinforced materials. Compos Part A 38(11):2333–2341.
[39] Liu, K.S., Tsai, S.W. (1998) A progressive quadratic failure criterion of a laminate. Compos Sci Technol. 58:102332.
[40] Liu, P.F., Gu, Z.P., Yang, Y.H., Pengb, X.Q. (2016) A nonlocal finite element model for progressive failure analysis of composite laminates. Composites Part B, 86:178–196.
[41] Lubineau, G., Ladeveze, P. (2008) Construction of a micromechanics-based intralaminar mesomodel, and illustrations in ABAQUS/Standard. Comput Mater Sci 43(1):137–145.
[42] Lubarda, V.A., Krajcinovic, D. (1993) Damage Tensors and the Crack Density Distribution. International Journal of Solids Structures, 30, 2859–2877.
[43] Maimí, P., Camanho, P.P., Mayugo, J.A., Dávila, C.G. (2007) A continuum damage model for composite laminates: part I constitutive model. Mech Mater 39:897908
[44] Maimí, P., Camanho, P.P.,, Mayugo, J.A., Dávila, C.G. (2006) A continuum damage model for composite laminates: part II computational implementation and validation. Mech Mater 39:909–919.
[45] Matzenmiller, A., Lubliner, J., Taylor, R.L. (1995) A constitutive model for anisotropic damage in fiber-composites. Mech. Mater. 20:125–152.
[46] McCarthy M.A., McCarthy C.T., Lawlor V.P. (2005) Progressive damage analysis of multi-bolt composite joints with variable bolt-hole clearances . Composites Part B Engineering, 36:290-305.
[47] Menzel, A., Steinmann, P. (2001) A theoretical and computational framework for anisotropic continuum damage mechanics at large strains. International Journal of Solids and Structures, 38:9505–9523.
[48] Menzel, A. Ekh, M., Steinmann, P., Runesson, K. (2002) Anisotropic damage coupled to plasticity: Modelling based on the effective configuration concept. International Journal for Numerical Methods in Engineering, 54(10):1409–1430.
[49] Mori, T., Tanaka, K. (1973) Average stress in the matrix and average elastic energy of materials with misfitting inclusions. Acta Metall 21:571574.
[50] de Moura, M.F.S.F., Campilho, R.D.S.G., Amara, A.M., Reis, P.N.B. (2010) Interlaminar and intralaminar fracture characterization of composites under mode I loading. Compos Struct 92:144-149.
[51] Peerlings, R., Geers, M.G.D., de Borst, R., Brekelmans W. (2001) A critical comparison of non local and gradient-enhanced softening continua. Int. J. Solids Struct. 38:77237746.
[52] Pinho, S.T., Dávila, C.G., Camanho, P.P., Ianucci, L., Robinson, P. (2004) Failure models and criteria for FRP under in-plane or three-dimensional stress states including shear non-linearity. NASA/TM-2003–213530.
[53] Pinho, S.T., Iannucci, L., Robinson, P. (2006) Physically-based failure models and criteria for laminated fibre-reinforced composites with emphasis on fibre kinking: part I: development. Composites: Part A 37:63–73.
[54] Pinho, S.T., Robinson, P., Iannucci, L. (2006) Fracture toughness of the tensile and compressive fibre failure modes in laminated composites. Compos Sci Technol 66(13):2069–2079.
[55] Puck, A., Schürmann, H. (1998) Failure analysis of frp laminates by means of physically based phenomenological models. Compos Sci Technol, 58:1045–1067.
[56] Puck, A., Schürmann, H. (2002) Failure analysis of frp laminates by means of physically based phenomenological models. Compos Sci Technol, 62:16331662.
[57] Rah K, Van Paepegem W, Habraken A-M, Degrieck J, de Sousa RA, Valente, RAF (2013) Optimal low-order fully integrated solid-shell elements. Comput Mech 51(3):309326.
[58] Reinoso J., Blázquez A., Estefani A., París F., Cañas,J., Arévalo E., Cruz F. Experimental and three-dimensional global-local finite element analysis of a composite component including degradation process at the interfaces. Composites: Part B, 2012:43:1929–1942.
[59] Reinoso J., Blázquez A., Estefani A., París F., Cañas J. A composite runout specimen subjected to tension-compression loading conditions: experimental and global-local finite element analysis. Compos. Struct., 2013,101:274–289.
[60] Reinoso, J., Blázquez, A. (2016) Application and finite element implementation of 7-parameter shell element for geometrically nonlinear analysis of layered CFRP composites. Composite Structures, 139:263–276.
[61] Reinoso, J., Paggi, M., Areias, P. (2016) A finite element framework for the interplay between delamination and buckling of rubber-like bi-material systems and stretchable electronics. J Eur Ceram Soc 36 (9), 2371–2382.
[62] Reinoso, J., Blázquez, A. (2016) Geometrically nonlinear analysis of functionally graded power-based and carbon nanotubes reinforced composites using a fully integrated solid shell element. composite Structures, 152:277–294.
[63] Reinoso, J., Paggi, M. Linder, C. (2017) Phase field modeling of brittle fracture for enhanced assumed strain shells at large deformations: formulation and finite element implementation. Computational Mechanics 6 (59), 981–1001.
[64] Reinoso, J., Paggi, M. Blázquez, A. (2017) A nonlinear finite thickness cohesive interface element for modeling delamination in fibre-reinforced composite laminates, Composites Part B: Engineering, 109, 116–128.
[65] Schuecker, C., Pettermann, H.E., (2006) A continuum damage model for fiber reinforced laminates based on ply failure mechanisms. Composite Structures 76, 162–173.
[66] Schwarze, M., Reese, S. (2009) A reduced integration solid-shell finite element based on the EAS and the ANS concept-

geometrically linear problems. Int J Numer Methods Eng 80:1322–1355.
[67] Simo, J.C, Ju, W. (1987) Stress and strain-based continuum damage model I. Formulation, II. Computational aspects. International Journal of Solids and Structures, 23: 821–869.
[68] Simo, J.C., Armero, F. (1992) Geometrically nonlinear enhanced strain mixed methods and the method of incompatible modes. Int J Numer Methods Eng 33:1413–1449.
[69] Sun, C.T., Tao, J.X. (1998) Prediction of failure envelopes and stress strain behaviours of composite laminates. Compos Sci Technol, 58:112536.
[70] Tandon, G.P., Weng, G.J. (1984) The effect of aspect ratio of inclusions on the elastic properties of unidirectionally aligned composites. Polym Compos 5:327–333
[71] Tsai, S.W., Wu, E.M. (1971) A general theory of strength for anisotropic materials. J Compos Mater, 5:58–80.
[72] Tserpes K.I., Labeas G., Papanikos P., Kermanidis Th. Strength prediction of bolted joints in graphite/epoxy laminates. Composites Part B: Engineering, 2002, 33:521–529.
[73] Van Der Meer, F.P., Sluys, L.J. (2009) Continuum models for the analysis of progressive failure in composite laminates, J. Compos. Mater 43(20):2131–2156.
[74] Vogler, M., Rolfes, R., Camanho, P.P. (2013) Modeling the inelastic deformation and fracture of polymer compositese Part I: plasticity model. Mech. Mater 59:50–64.
[75] Voyiadjis G.Z., Taqieddin Z.N., Kattan, P.I. (2008) Anisotropic damage-plasticity model for concrete. International Journal of Plasticty, 24:1946–1965.
[76] Wagner, W., Balzani, C. (2010) Prediction of the postbuckling response of composite airframe panels including ply failure, Engineering Fracture Mechanics 77(18):3648-3657
[77] Vu-Quoc L, Tan XG. (2003) Optimal solid shells for non-linear analysis of multilayer composites. Part I: Statics. Computer Methods in Applied Mechanics and Engineering 192:975–016.
[78] Open hole tensile strength of polymer composite laminates, ASTM D 5766/D 5766M-02a. West Conshohocken (PA), USA: American Society for Testing and Materials (ASTM).